SIMULATIONS OF TOPOLOGICAL DEFECTS AND IMPURITIES IN SUPERFLUID ^{3}HE

Risto Hänninen

TEKNILLINEN KORKEAKOULU
TEKNISKA HÖGSKOLAN
HELSINKI UNIVERSITY OF TECHNOLOGY
TECHNISCHE UNIVERSITÄT HELSINKI
UNIVERSITE DE TECHNOLOGIE D'HELSINKI

SIMULATIONS OF TOPOLOGICAL DEFECTS
AND IMPURITIES IN SUPERFLUID ^{3}HE

Risto Hänninen

HELSINKI UNIVERSITY OF TECHNOLOGY P.O. BOX 1000, FIN-02015 HUT http://www.hut.fi	ABSTRACT OF DOCTORAL DISSERTATION

Author Risto Matias Hänninen	

Name of the dissertation

SIMULATIONS OF TOPOLOGICAL DEFECTS AND IMPURITIES IN SUPERFLUID ^{3}HE

Date of manuscript 10.6.2003	Date of the dissertation 3.10.2003
☐ Monograph	☑ Article dissertation (summary + original articles)

Department	Department of Engineering Physics and Mathematics
Laboratory	Low Temperature Laboratory
Field of research	Theoretical low temperature physics
Opponent(s)	Prof. Dierk Rainer
Supervisor	Prof. Martti M. Salomaa
(Instructor)	Prof. Erkki V. Thuneberg

Abstract

The less common helium isotope, ^{3}He, becomes superfluid when the temperature falls below 1 mK. Superfluidity is one indication of a condensation into the same quantum mechanical state. For ^{3}He the condensation into a single state occurs by forming Cooper pairs. In the superfluid state ^{3}He is an ideal substance to study a non-conventional p-wave spin-triplet pairing. This dissertation considers theoretically different topological defects that appear in the superfluid state and the effect of impurities.

Vortices and solitons are the most common topological defects that appear in superfluid ^{3}He. They may be observed in both A and B phases by using nuclear magnetic resonance (NMR). Here we consider the A phase vortex texture in the presence of a stable A-B phase boundary. As a result two new possible vortex textures were obtained to exist at the A-B boundary. Both of these surface sheet textures differ from the vortex sheet that appears in the bulk A phase. Different dissipation mechanisms are analyzed by calculating the NMR absorption spectrum caused by solitons. The normal-superfluid relaxation causes only line broadening, but the spin diffusion, which results from the inhomogeneous texture, also shifts the soliton peak to higher frequencies.

Typically helium is an ultra-pure liquid without any impurities. Experimentally the effect of impurities on the superfluid state can be investigated by using a very porous aerogel. When the empty space inside aerogel is filled with liquid helium, the aerogel strands act as an impurity and scatter the helium quasiparticles. In this thesis the effect of impurities on superfluid ^{3}He is analyzed by using the quasiclassical theory and by considering two simple scattering models. In the homogeneous scattering model the impurities are assumed to be evenly distributed, the assumption that is often used for superconductors. In the inhomogeneous model the impurity density is allowed to depend on location. Using these models the critical temperature, pair amplitude, and superfluid density for ^{3}He are determined numerically.

Keywords helium-3, superfluidity, texture, vortex, soliton, impurity, hydrodynamic theory, quasiclassical theory	

Acknowledgments

Otaniemi, May 2003

Risto Hänninen

List of publications

This thesis is based on the following original publications.

[P1] R. Hänninen, R. Blaauwgeers, V. B. Eltsov, A. P. Finne, M. Krusius, E. V. Thuneberg, and G. E. Volovik, *Structure of surface vortex sheet between two rotating ^3He superfluids*, Phys. Rev. Lett. **90**, 225301-1–4 (2003). © 2003 by the American Physical Society.

[P2] J. Kopu, R. Hänninen, and E. V. Thuneberg, *One-dimensional textures and critical velocity in superfluid ^3He-A*, Phys. Rev. B **62**, 12374–12380 (2000). © 2000 by the American Physical Society.

[P3] R. Hänninen and E. V. Thuneberg, *Calculation of NMR properties of solitons in superfluid ^3He-A*, Phys. Rev. B **68**, 094504-1–11 (2003). © 2003 by the American Physical Society.

[P4] R. Hänninen, T. Setälä, and E. V. Thuneberg, *Homogeneous scattering model for impure superfluid ^3He*, Physica B **255**, 11–18 (1998). © 1998 by Elsevier.

[P5] R. Hänninen and E. V. Thuneberg, *Superfluid density for ^3He in aerogel assuming inhomogeneous scattering*, Physica B **284**, 303–304 (2000). © 2000 by Elsevier.

[P6] R. Hänninen and E. V. Thuneberg, *Model of inhomogeneous impurity distribution in Fermi superfluids*, Phys. Rev. B **67**, 214507-1–11 (2003). © 2003 by the American Physical Society.

Author's contribution

The research reported in this thesis was done together with my thesis instructor, Prof. Erkki Thuneberg, and in collaboration with other co-authors. In publication [P1] I did the theoretical texture calculation described in section *"Structure of surface vortex sheet"* and in [P2] I did the analytical stability analysis described at the beginning of Sec. IV. Excluding the effect of the higher partial waves for the B phase, I did most of the numerical work represented in publication [P4]. For publications [P3], [P5], and [P6] I did all the numerical calculations. In all cases the numerical implementation required a lot of analytical work to produce the final equations for solution and programming. I wrote the first versions of publications [P3], [P5], and [P6] and also contributed to the iterative writing process of all papers.

Contents

1 Introduction

At low temperatures both stable helium isotopes, ^{3}He and the more common isotope ^{4}He, are liquids. At normal pressures they remain liquids even at absolute zero temperature. However, near the absolute zero one starts to observe superfluidity, a flow without friction. For ^{4}He the transition temperature to superfluid state is about 2 K and for ^{3}He it is only about 1 mK. Superfluidity is similar to superconductivity in metals, where the electric current flows without resistance. In this thesis I concentrate on the theoretical studies of superfluid ^{3}He. Theories created for superconductors can often be applied also for ^{3}He. Since the order parameter for ^{3}He is more complex than for typical superconductors there exist various phenomena that cannot be observed in superconductors.

The superfluidity in ^{3}He was first observed at the beginning of the 1970's by Osheroff *et al.* [1] and since then it has been studied extensively. In the superfluid state, depending on external parameters (temperature, pressure and magnetic field) three types of phases have been observed. They all have different physical properties due to dissimilar internal symmetries. In all phases one may observe various topological defects. The most common defects are vortices that appear when the superfluid is put into rotation. Vortices are linear objects aligned along the rotation axis, and surrounded by a circulating flow. They are similar to vortices in superfluid ^{4}He and in superconductors. The vortices and other defects in ^{3}He may be observed by using the nuclear magnetic resonance (NMR) which is an important tool for analyzing the state of superfluid ^{3}He.

Typically ^{3}He is an ultra-pure liquid since all the impurities are adsorbed on the walls of the container. This enables us to investigate the substance itself and not to worry about complications caused by impurities. For example, by applying a pressure of some 34 bar, one may solidify the liquid and observe the growth and shrink process of an almost perfect crystal. However, also the impurities may give us information about the superfluid itself. In ^{3}He the adding of impurities may be done using silica aerogel. Aerogel has a spaghetti-like structure, where only a few nanometer thick, long silica strands form a self-supporting structure that has a large open volume, even up to 99.5%. These aerogel strands scatter the helium quasiparticles and act as an impurity when the open volume is filled with superfluid ^{3}He. Impurities cause the superfluid condensate to be reduced but not necessary totally suppressed.

Even if the behavior of superfluid ^{3}He is complex, it is very well understood. The theories are well developed and they often agree with the experiments quantitatively. Nowadays the remaining unsolved theoretical

problems are often too difficult to be solved by analytical methods and numerics is needed. The problems presented in the thesis are mainly solved by using different numerical methods and computers.

This thesis is divided into two parts. In the first part I concentrate on the hydrodynamic theory which can be used to calculate different textures on the length scales that are much larger than the coherence length $\xi_0 \approx 50$nm. This part also includes a short introduction to NMR in Sec. 3. The second part of the thesis, described in Sec. 4, contains a short introduction to the quasiclassical theory of ^{3}He. This theory is used to calculate the effect of impurities by considering two simple scattering models.

1.1   Order parameter in ^{3}He

Superfluidity in helium is one indication of the condensation where particles start to occupy the same macroscopic quantum state. In contrast to ^{4}He atoms, which are bosons, the ^{3}He the atoms are fermions which cannot occupy the same state. Therefore it is not the atoms that have the same wave function but the bosonic Cooper pairs formed by two helium atoms. These Cooper pairs are in the p-wave spin-triplet state with orbital angular momentum $L = 1$ and spin $S = 1$ [2–5]. This implies that, in general, nine complex amplitudes are needed to determine the actual state. Typically the order parameter is represented by using a complex 3×3 matrix $A_{\mu j}$, where the first index μ refers to the spin and the second index j to orbital degrees of freedom.

The observed superfluid phases correspond to specific forms of the general matrix. The phase diagram for ^{3}He is illustrated in Fig. 1. In the absence of magnetic field the most stable phase at low pressures (below 21 bar) and also at higher pressures at low temperatures is the B phase. For B phase the order parameter has the form [4–6]

$$A_{\mu j} = \Delta_{\mathrm{B}} e^{i\varphi} R_{\mu j} \ . \tag{1}$$

Here $R_{\mu j}$ is a rotation matrix in three dimensions and the real parameter Δ_{B} is the pair amplitude that determines the energy required to break one Cooper pair. For the A phase, which is stable at high pressures at temperatures near the superfluid transition temperature T_{c}, the order parameter is given by [4, 5, 7]

$$A_{\mu j} = \Delta_{\mathrm{A}} \hat{d}_\mu (\hat{m}_j + i\hat{n}_j), \tag{2}$$

where $\hat{\mathbf{m}} \perp \hat{\mathbf{n}}$. Here the unit vector $\hat{\mathbf{l}} = \hat{\mathbf{m}} \times \hat{\mathbf{n}}$ defines the axis of the orbital angular momentum of a Cooper pair and $\hat{\mathbf{d}}$ defines the spin axis. The phase factor $\exp(i\varphi)$, seen in the B phase order parameter, is hidden in the orbital
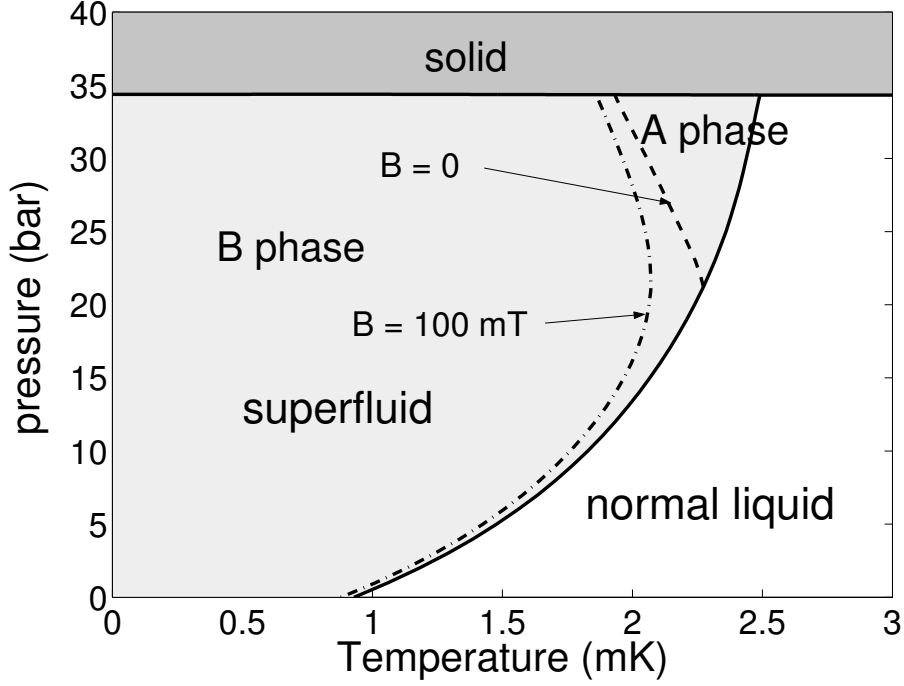
Figure 1: Phase diagram for ^{3}He at low temperatures. The dashed line denotes the A-B phase boundary at zero magnetic field and the dash-dotted line for $B = 100$ mT. The region for stable A_1 phase, just below T_c, is so thin that it is not observable in this scale.

triad $\{\hat{\mathbf{l}}, \hat{\mathbf{m}}, \hat{\mathbf{n}}\}$. In the presence of external magnetic field the stability region of the A phase extends to lower temperatures and also to lower pressures. At the same time there appears a thin region of A_1 phase just below T_c. The A_1 phase differs slightly from the A phase.

Typically the superfluids can be analyzed by using a phenomenological two-fluid model where the liquid is a mixture of normal viscous fluid, with density ρ_n and velocity $\mathbf{v}_n$, and superfluid. The superfluid has velocity of $\mathbf{v}_s$ and a density of $\rho_s = \rho_{tot} - \rho_n$, where ρ_{tot} is the total density of the fluid. For the B phase the superfluid velocity is given by

$$\mathbf{v}_s = \frac{\hbar}{2m_3} \nabla \varphi \ , \tag{3}$$

where φ is the phase in the order parameter, m_3 is the mass of ^{3}He atom and $\hbar = h/2\pi$ is Planck's constant. Since the flow is potential, the vorticity vanishes, $\nabla \times \mathbf{v}_s = 0$. This is not valid, for example, at the vortex cores where the order parameter is not of the simple form as above in Eq. (1) [8–10]. The

3

diameter of the vortex core is determined by the coherence length ξ, which for ^{3}He is typically around 50 nm. Around a vortex the circulation

$$\kappa = \oint d\mathbf{r} \cdot \mathbf{v}_s = \frac{\hbar}{2m_3} \oint d\mathbf{r} \cdot \nabla\varphi = n\frac{h}{2m_3} = n\kappa_0 \qquad (4)$$

is a multiple of the circulation quantum $\kappa_0 = h/(2m_3)$. The vortices in the B phase are typically one quantum vortices with $n = 1$. This minimizes the kinetic energy. In the A phase the superfluid velocity is given by

$$\mathbf{v}_s = \frac{\hbar}{2m_3} \sum_i m_i \nabla n_i \qquad (5)$$

and there exist many different types of vortices. Now there is no such restriction for the vorticity $\nabla \times \mathbf{v}_s$, and the order parameter can retain its bulk form, given by Eq. (2), also inside the vortex core. These continuous vortices are typically much larger in diameter than the B phase vortices and are mostly two-quantum vortices. Inside the core the circulation can have, in principle, any value. In the anisotropic A phase the superfluid density ρ_s is no longer a scalar, but depends on the orientation of the $\hat{\mathbf{l}}$ vector with respect to the superfluid velocity.

2 Hydrostatic theory

Within the hydrostatic theory the free energy of superfluid ^{3}He may be written as a expansion in spatial gradients of the order parameter. The hydrostatic theory is valid at general temperature $T < T_c$. The external perturbations, a magnetic field and an applied flow for example, are assumed to be so small that the order parameter sustains its bulk form, where the amplitude Δ is fixed by temperature and pressure. In the A phase the leading terms in the free-energy density are the magnetic and dipole terms together with the gradient energy density [5, 11, 12]. The dipole term

$$f_d = -\frac{1}{2}\lambda_d(\hat{\mathbf{d}} \cdot \hat{\mathbf{l}})^2, \tag{6}$$

measures the strength of the dipole-dipole interaction between nuclear moments and favors $\hat{\mathbf{l}} \parallel \hat{\mathbf{d}}$. The magnetic term

$$f_h = \frac{1}{2}\lambda_h(\hat{\mathbf{d}} \cdot \mathbf{B})^2 , \tag{7}$$

describes the coupling to the external field $\mathbf{B}$ and prefers to have $\hat{\mathbf{d}} \perp \mathbf{B}$. The gradient energy density f_g, where

$$
\begin{aligned}
2f_g &= \rho_\perp(\mathbf{v}_s - \mathbf{v}_n)^2 + (\rho_\parallel - \rho_\perp)(\hat{\mathbf{l}} \cdot (\mathbf{v}_s - \mathbf{v}_n))^2 + 2C(\mathbf{v}_s - \mathbf{v}_n) \cdot \boldsymbol{\nabla} \times \hat{\mathbf{l}} \\
&- 2C_0\hat{\mathbf{l}} \cdot (\mathbf{v}_s - \mathbf{v}_n)(\hat{\mathbf{l}} \cdot \boldsymbol{\nabla} \times \hat{\mathbf{l}}) + K_s(\boldsymbol{\nabla} \cdot \hat{\mathbf{l}})^2 + K_t(\hat{\mathbf{l}} \cdot \boldsymbol{\nabla} \times \hat{\mathbf{l}})^2 \\
&+ K_b|\hat{\mathbf{l}} \times (\boldsymbol{\nabla} \times \hat{\mathbf{l}})|^2 + K_5|(\hat{\mathbf{l}} \cdot \boldsymbol{\nabla})\hat{\mathbf{d}}|^2 + K_6\sum_{i,j}[(\hat{\mathbf{l}} \times \boldsymbol{\nabla})_i\hat{\mathbf{d}}_j]^2, \tag{8}
\end{aligned}
$$

contains also the kinetic energy arising from the counterflow velocity $\mathbf{v} = \mathbf{v}_s - \mathbf{v}_n$. Now the characteristic length scale is the dipole length $\xi_d = (\hbar/2m_3)\sqrt{\rho_\parallel/\lambda_d} \approx 10~\mu$m, which is much larger than the coherence length and is obtained by comparing the dipole and kinetic terms. Similarly comparing the dipole and magnetic terms one obtains the dipole field $B_d = \sqrt{\lambda_d/\lambda_h} \approx 2$ mT. All the coefficients appearing in the energy density are positive and have been calculated in the weak-coupling approximation [13–15].

Similarly in the B phase one may write the free energy using the rotation matrix $R_{\mu j}$ and the phase φ. An extensive introduction to hydrostatics in the B phase is given in Ref. [16]. Since there are no B phase texture calculations presented in this thesis the explicit form of the different energy terms is omitted. However, some main points should be noted: In the B phase the conservation of the mass current fixes $\nabla^2\varphi = 0$. Together with the boundary conditions this already determines φ. Additionally the dipole-dipole interaction between the ^{3}He atoms favors that the rotation angle in $R_{\mu j}$ is fixed to

$\theta = \arccos(-1/4) \approx 104°$. As a result, spin currents are not conserved but decay on the scale ξ_d. The remaining energy terms determine the rotation axis for $R_{\mu j}$. The variation of this axis typically takes place on the length scale that is much larger than ξ_d and therefore one must usually take into account the form of the helium container, whose diameter is normally a few millimeters.

2.1 A-B phase boundary

In both superfluid phases there exist several different textures and topological defects. The most common of such defects are vortices. They are created when the counterflow velocity exceeds some critical value [17]. An interesting situation occurs when one has two separate phases, both with different internal symmetries, at different parts of the sample and a thin phase boundary between these regions. This phase separation can be achieved, for example, by having a non-uniform magnetic field. If a topological object penetrates through this boundary, its structure is usually modified.

In publication [P1] we calculate the structure of the A phase vortex in the presence of the A-B phase boundary. The calculations were motivated by recent experiments where the A-B phase boundary is stabilized in the middle of the long cylinder by having an axial magnetic field whose magnitude is peaked at the half way of the cylinder [18]. The large magnetic field prevents the B phase from filling the whole cell when the sample is cooled. In the upper part of the cell the A phase remains in the metastable supercooled state.

When one starts to rotate the experimental cell, the vortices first appear in the A phase since the critical velocity for creating vortices is considerably smaller there than in the B phase. In order to minimize the kinetic energy the vortices form a vortex bundle at the center of the cylinder, such that on average $\langle v_s \rangle \approx v_n$ inside the vortex bundle. Since the continuous unlocked vortices in the A phase have a large soft core and the number of circulation is two times the circulation quantum, it is hard for these vortices to penetrate to the B phase where vortices carry only one quantum of circulation and have a small singular core. So, instead of going through the phase boundary, the vortices bend along the boundary and terminate at the edge of the cell as illustrated in Fig. 2. We are especially interested in this case where no vortices are present in the B phase, *i.e.* the superfluid component is still at rest in the laboratory frame. For large enough rotation velocities the vortices start to penetrate to the B phase and the mechanism involves the classical Kelvin-Helmholtz instability [18].

Mathematically, the boundary condition at the A-B phase boundary may
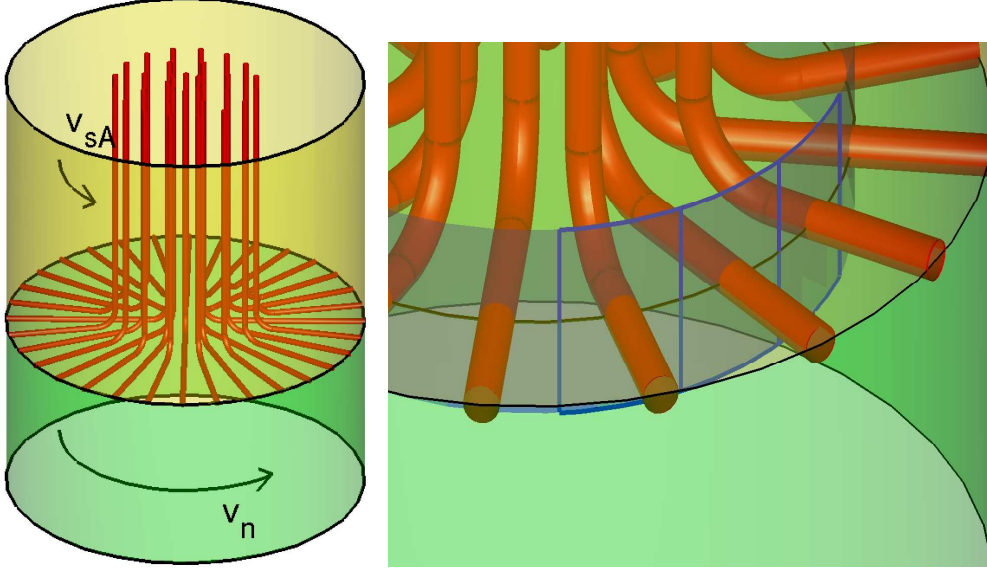
Figure 2: *Left:* Behavior of the A-phase vortices in the presence of the phase boundary. The upper part of the cell is in A phase state where the vortices create a nonzero superfluid velocity. The lower part is in a vortex-free B phase state where the superfluid part is at rest and only the normal fluid rotates with the cell. *Right:* Calculation area used to determine the texture is denoted by rectangles. Periodicity along the azimuthal angle is assumed.

be written as [19–21]

$$\hat{\mathbf{d}} = \pm\overleftrightarrow{R} \cdot \hat{\mathbf{s}} \tag{9}$$

$$(\hat{\mathbf{m}} + i\hat{\mathbf{n}}) \cdot \hat{\mathbf{s}} = \pm e^{i\varphi} \tag{10}$$

$$\hat{\mathbf{l}} \cdot \hat{\mathbf{s}} = 0, \tag{11}$$

where $\hat{\mathbf{s}}$ is the normal of the A-B boundary, φ is the phase and $\overleftrightarrow{R}$ the rotation matrix appearing in the B-phase order parameter. Here the second equation states that the phase angle is continuous across the A-B boundary. The last equation indicates that the $\hat{\mathbf{l}}$ vector lies parallel to the A-B boundary. This differs from the behavior near the walls where the $\hat{\mathbf{l}}$ vector is forced to be normal to the walls.

   If one considers the region outside the vortex bundle at some constant distance from the cylinder axis shown in Fig. 2 and ignores the small curvature, one obtains the following simplified 2D model for the calculations: the A-B phase boundary resides at $z = 0$ and there is a periodic structure along the

y-axis (the azimuthal axis) with period of L_y. In the x direction (the radial direction) we have translational invariance. In reality, these are true only approximately, but they give a simple model to examine the effect of the phase boundary. Far below the phase boundary ($z \to -\infty$), deep in the B phase, we have no vortices and the superfluid velocity is zero. Therefore the counterflow velocity is only due to the normal fluid velocity ($\mathbf{v}_B = \mathbf{v}_{sB} - \mathbf{v}_n = -\mathbf{v}_n$). Deep in the A phase the counterflow velocity $\mathbf{v}_A = \mathbf{v}_{sA} - \mathbf{v}_n$ is, due to vortices, considerably smaller than $\mathbf{v}_B$. In the calculations we used $\mathbf{v}_A = 0$. This is appropriate when we consider a region that is not far from the vortex bundle. The circulation of two quanta inside the calculation area is ensured by having $\mathbf{v}_B = 2\kappa_0 \hat{\mathbf{y}}/L_y$ deep in the B phase.

The characteristic length scale for the rotation matrix $\overset{\leftrightarrow}{R}$ in the B phase is typically much larger than the characteristic length scale (dipole length ξ_d) in the A phase. Therefore the variation in rotation matrix can only result from the boundary condition for $\hat{\mathbf{d}}$, given by Eq. (9). Since, even with a free boundary condition, we obtain that $\hat{\mathbf{d}} \approx \hat{\mathbf{y}}$ also at the boundary, the rotation matrix was chosen to be constant, such that $\hat{\mathbf{d}} = \hat{\mathbf{y}}$ at the phase boundary. This simplifies the calculations, and we only have to take into account the B-phase kinetic energy in the form

$$f_B = \frac{1}{2}\rho_s(\mathbf{v}_{sB} - \mathbf{v}_n)^2. \tag{12}$$

This term is required to stabilize the vorticity at the phase boundary.

The texture near the phase boundary is obtained by discretizing the calculation area ($0 \leq y \leq L_y$ and $-L_z \leq z \leq L_z$) into $2N_y N_z$ points and taking the phase field φ and the five angles needed to define the vectors $\hat{\mathbf{d}}$, $\hat{\mathbf{m}}$ and $\hat{\mathbf{n}}$ at these discrete points to be the minimization variables. At the A-B boundary only one angle in addition to φ is needed. Minimization was done using the conjugate gradient method. As an initial guess a continuous unlocked vortex or one period of vortex sheet was used on the A-phase side.

As a result two new types of textures were found. For large L_y, or equivalently at small counterflow velocities, the vorticity separates into two composite one-quantum vortices that are aligned on the A-B boundary as illustrated in Fig. 3. These one-quantum vortices consist of two half-quantum cores where $\hat{\mathbf{l}} = \pm\hat{\mathbf{x}}$. For larger counterflow velocities ($L_y \leq 5.7\xi_d$) a more stable configuration consists of two half-quantum cores at the boundary and the remaining circulation appearing as a one-quantum vortex between these cores above the phase boundary as shown in Fig. 4. The obtained textures seem to be independent of the initial ansatz, $i.e.$ whether a normal vortex or a period of bulk vortex-sheet is used as the initial texture. Transition be-
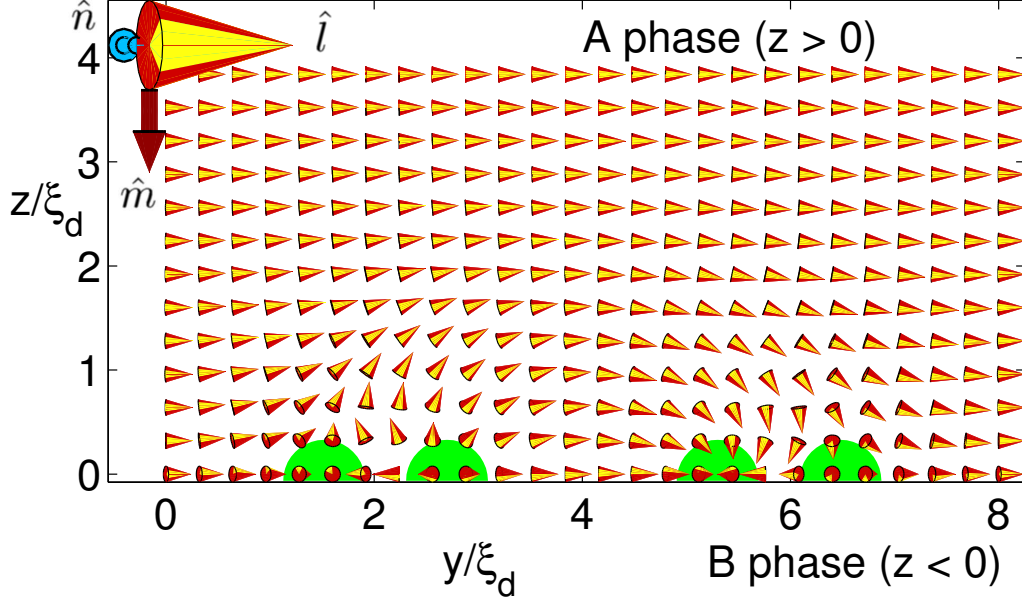
Figure 3: Low-density texture on the A phase side when $L_y = 8\xi_d$ in the coordinate system where $v_n = 0$. The light strip in the cones denotes the rotation of the $\hat{\mathbf{m}}$ and $\hat{\mathbf{n}}$ vectors around $\hat{\mathbf{l}}$, as indicated in the upper-left corner. The texture contains two separate one-quantum vortices, both with two half-quantum cores at the phase boundary aligning perpendicular to the plane of the paper (along the x-axis). The cores are denoted by shading and at the cores $\hat{\mathbf{l}} = \pm\hat{\mathbf{x}}$. In the left-side one-quantum vortex vector $\hat{\mathbf{l}}$ sweeps the upper hemisphere with $l_z > 0$ and in the right-side vortex the hemisphere with $l_z < 0$. The B phase texture at $z < 0$ is not illustrated here but there the phase field φ is only slightly distorted from bulk value ($\varphi \propto y + \text{const}$) near the vortex cores.

tween these two textures seems to be hysteretic, especially the high-density texture can remain stable at least up to $L_y \approx 7.5\xi_d$.

The experimental identification of the texture at the phase boundary is quite difficult. The magnetic field at the phase boundary is strongly inhomogeneous. This complicates the analysis of the NMR absorption signal since the Larmor frequency $\omega_0 = \gamma B_0$ depends on the location (for details about the NMR, see the next section). The surface layer is also very thin, so that the absorption signal is weak and most likely covered by the signal caused by the bulk vortices. The experimentally measured velocity where the phase boundary becomes unstable is only slightly larger than the value where the high-density texture becomes stable. The calculations were done near the polycritical point, a region were $T = T_c$, $p \approx 21$ bar and $B = 0$, and the re-
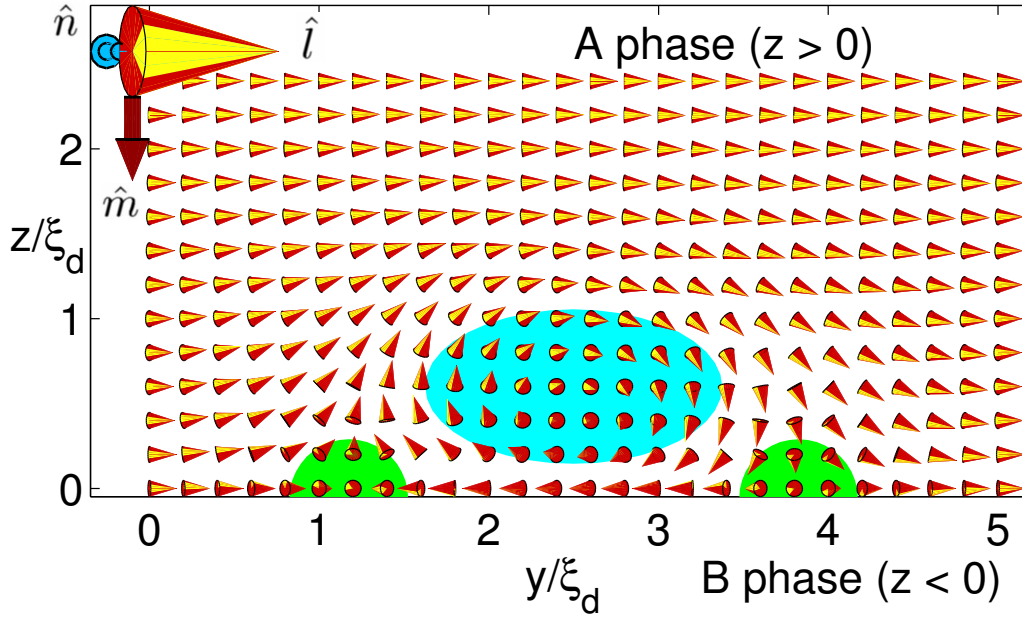
Figure 4: High-density texture on the A phase side when $L_y = 5\xi_{\mathrm{d}}$ in the coordinate system where $v_{\mathrm{n}} = 0$. The circulation is divided into two half-quantum cores at the phase boundary bounded together by the remaining one-quantum vortex in the vicinity of the phase boundary. The vortex cores are denoted by shading. At the half-quantum cores $\hat{\mathbf{l}} = -\hat{\mathbf{x}}$.

sults might change slightly if the correct experimental parameters were used. At least for low rotational velocities the texture should be the low-density one.

After the phase boundary becomes unstable and some of the vortices penetrate into the B phase, one may calculate the number of penetrated vortices by NMR. This number is observed to be a small random number and it may be even or odd. When the number is odd it means that only one half of an A-phase vortex has penetrated to the B phase. This appears to be realized more easily with the low-density texture which has two separate one-quantum vortices at the phase boundary and then only one of them penetrates through the boundary. However, the penetration is a non-equilibrium process and therefore considerable changes in texture may occur during this process.

2.2 Helical instability in ^{3}He-A

In case of vanishing counterflow velocity the minimum free energy is achieved with a uniform texture $\hat{\mathbf{l}} = \hat{\mathbf{d}} \perp \mathbf{B}$, which corresponds to a minimum of
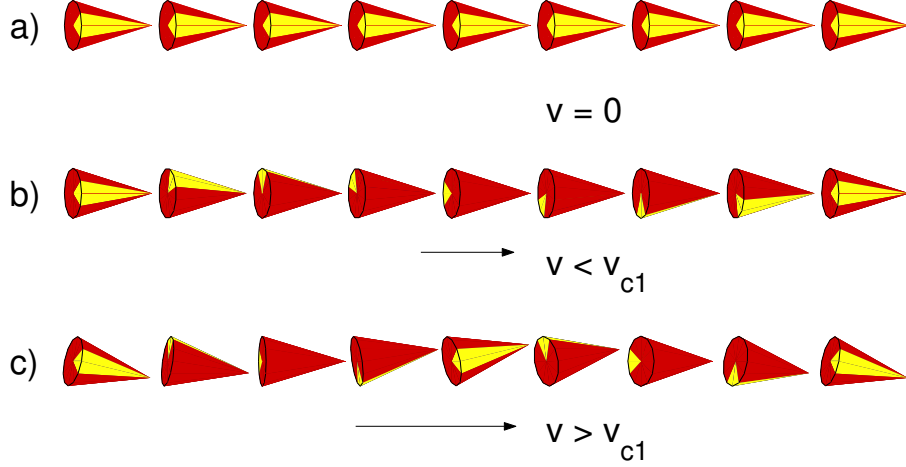
Figure 5: Principle of the helical instability in ^{3}He-A. The cones denote the direction of the $\hat{\mathbf{l}}$ vector and the light strip describes the rotation of $\hat{\mathbf{m}}$ and $\hat{\mathbf{n}}$ vectors around it.

all the energy terms (6), (7) and (8). This remains the minimum-energy texture also in the presence of a small counterflow velocity $\mathbf{v} \perp \mathbf{B}$. Since $\rho_\perp > \rho_\parallel$, the $\hat{\mathbf{l}}$ vector is additionally fixed parallel to the flow. The superfluid velocity, or the phase gradient, means that the vectors $\hat{\mathbf{m}}$ and $\hat{\mathbf{n}}$ start to rotate around $\hat{\mathbf{l}}$ as illustrated in Fig. 5b. When the counterflow velocity finally exceeds the first critical velocity v_{c1} the above constant texture no longer corresponds to the minimum of the free energy. In many cases the minimum-energy configuration is the so-called helical texture, where the $\hat{\mathbf{l}}$ vector, and due to dipole-dipole coupling also the $\hat{\mathbf{d}}$ vector, smoothly wind around the direction of the flow as illustrated in Fig. 5c. For the nonuniform $\hat{\mathbf{l}}$-texture the superfluid mass current is no longer a simple gradient of the phase but given by

$$\mathbf{j}_s = \rho_\perp \mathbf{v}_s + (\rho_\parallel - \rho_\perp)\hat{\mathbf{l}}(\hat{\mathbf{l}} \cdot \mathbf{v}_s) + C\nabla \times \hat{\mathbf{l}} - C_0\hat{\mathbf{l}}(\hat{\mathbf{l}} \cdot \nabla \times \hat{\mathbf{l}}). \qquad (13)$$

In publication [P2] we analyze the stability of the helical texture both analytically and numerically. The dependence on temperature and magnetic field is analyzed. Previously most of the calculations were limited to the case where $\mathbf{B} \parallel \mathbf{v}$ (see publication [P2] for references). We consider a bit more complicated case where $\mathbf{B} \perp \mathbf{v}$. In this case the magnetic field introduces "hard" and "easy" directions for the variations of the $\hat{\mathbf{d}}$ vector. Therefore the helix is elliptically distorted. This situation arises, for example, in a rotating cylinder when the magnetic field is along the rotation axis, which is often the most relevant orientation in the experiments.

11
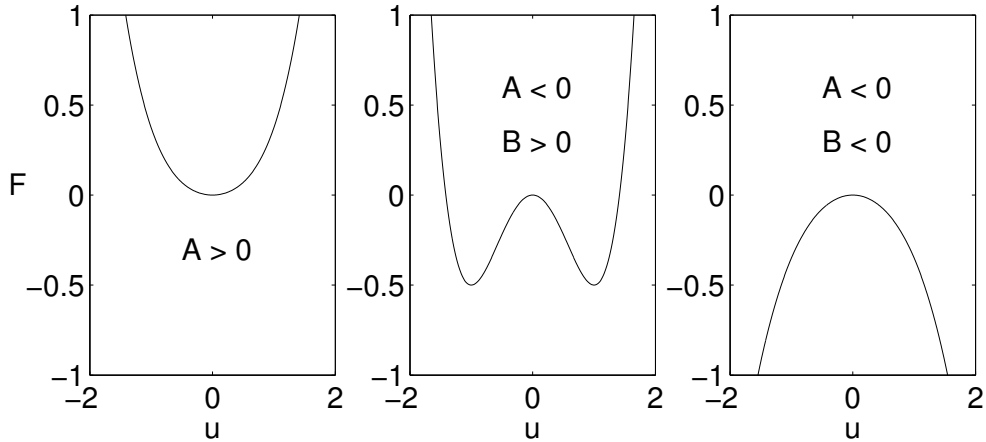
Figure 6: Stability analysis for the uniform and helical textures when $F = Au^2 + \frac{1}{2}Bu^4$. *Left:* Stable uniform texture ($u = 0$). *Center:* Stable helical texture with amplitude $u^2 = -\frac{A}{B}$. *Right:* Both textures are unstable.

Analytical solution is based on the Taylor expansion around the constant configuration $\hat{\mathbf{l}} = \hat{\mathbf{d}} = \hat{\mathbf{x}}$ with respect to small fluctuations. At the energy minimum the free energy may eventually be expressed by using a single small parameter u. It describes the amplitude of the fluctuations around the constant configuration. The free energy takes the form

$$F = F_0 + Au^2 + \frac{1}{2}Bu^4, \tag{14}$$

where the coefficients A and B depend on external parameters (temperature, magnetic field, *etc.*). For $A > 0$ the uniform texture with $u = 0$ is stable. The helical texture is stable for $A < 0$ and $B > 0$ when the minimum energy is achieved for $u^2 = -\frac{A}{B}$. When both coefficients are negative both the uniform and helical textures are unstable. All these cases are illustrated in Fig. 6.

In publication [P2] we generalize the results obtained by Lin-Liu *et al.* in Ref. [22] at $T = T_c$ to lower temperatures. At $T = T_c$, for example, the helical texture is stable only for $B < 2.5B_d$, but the stability region is extended when the temperature is lowered. Finally when $T < 0.8T_c$, the helical texture is stable at all fields. Unstable helical textures are again seen when the temperature falls bellow $0.5T_c$. In the numerical calculations one is not limited to small-amplitude oscillations. Therefore one may analyze the texture at much larger counterflow velocities than v_{c1} and finally determine the critical velocity v_{c2}, the velocity where the helical texture becomes unstable. Most likely this instability leads to formation of continuous vortices.

3 NMR in ³He-A

3.1 Solitons in the A phase

Solitons are perhaps the simplest defects that can be observed in ³He-A. They consist of a plane that separates two bulk configurations. For example, for dipole-unlocked solitons, on one side of the soliton $\hat{\mathbf{d}} = \hat{\mathbf{l}}$ and on the other $\hat{\mathbf{d}} = -\hat{\mathbf{l}}$. Both of these configurations correspond to minimum of the dipole energy. In the simplest case the texture depends only on the coordinate perpendicular to the soliton plane. Depending on the direction of the static magnetic field relative to this plane, a soliton is called either a twist or a splay soliton. In publication [P3] we analyze the structure of the composite twist and splay solitons, where both $\hat{\mathbf{d}}$ and $\hat{\mathbf{l}}$ vectors are allowed to vary. The structure of these solitons is illustrated in Fig. 7. For the twist soliton the structure is analytically solvable [23], but the splay texture requires either a variational ansatz [23,24] or a direct numerical solution as done in publication [P3].

A useful method for determining the order-parameter texture in superfluid ³He is by using nuclear magnetic resonance (NMR), where in addition to a static field $\mathbf{B}_0$ one has a weak oscillating rf-field $\mathbf{B}_{\mathrm{rf}}$ present. In the normal state the resonance absorption occurs at the Larmor frequency $\omega_0 = \gamma B_0$. Here the parameter γ is the gyromagnetic ratio of the ³He nucleus. In the superfluid state the NMR response can be determined from the Leggett equations which couple the spin magnetization $\gamma\mathbf{S}$ to the spin part of the order parameter [25,26].

Typically in the B phase the absorption spectrum can be obtained directly from the calculated texture, but for the A phase one must explicitly solve the resulting eigenvalue equations. If we choose the large static magnetic field to be along the z-axis such that the equilibrium $\hat{\mathbf{d}}$, denoted by $\hat{\mathbf{d}}_0 = \hat{\mathbf{x}}\cos\theta + \hat{\mathbf{y}}\sin\theta$, is limited to the xy-plane and ignore the dissipation effects, the resonance frequencies can be obtained from the Schrödinger-type eigenvalue equations

$$(\mathcal{D} + U_\parallel)\psi_\parallel = \alpha_\parallel \psi_\parallel \tag{15}$$

$$(\mathcal{D} + U_\perp)\psi_\perp = \alpha_\perp \psi_\perp. \tag{16}$$

Here the operator $\mathcal{D}$ is defined by

$$\mathcal{D}f = -\frac{K_6}{\lambda_{\mathrm{d}}}\nabla^2 f - \frac{K_5 - K_6}{\lambda_{\mathrm{d}}}\boldsymbol{\nabla}\cdot\left[\hat{\mathbf{l}}(\hat{\mathbf{l}}\cdot\boldsymbol{\nabla})f\right] \tag{17}$$

and the potentials are given by

$$U_\parallel = 1 - l_z^2 - 2(\hat{\mathbf{l}}\times\hat{\mathbf{d}}_0)_z^2 \tag{18}$$

13
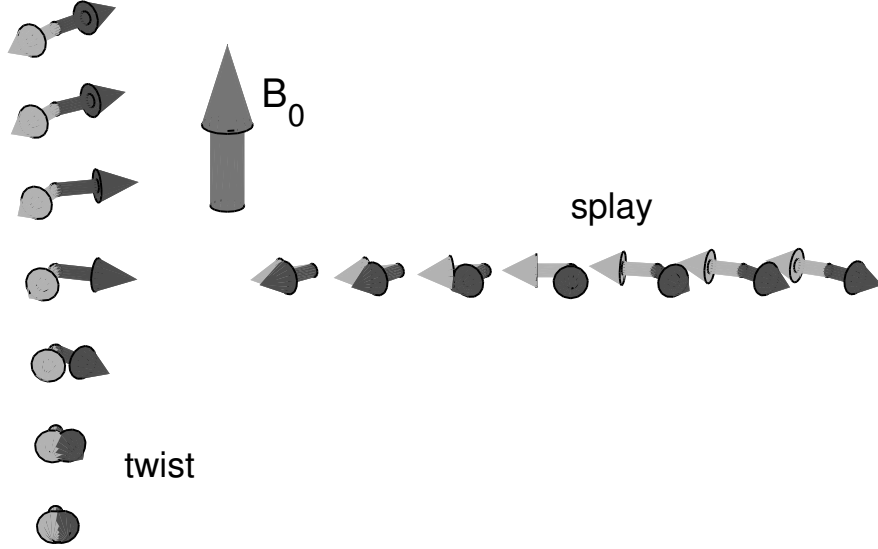
Figure 7: Structure of composite twist (left) and splay (right) solitons in superfluid ^{3}He-A in the absense of the flow. The darker arrows indicate the $\hat{\mathbf{l}}$ vector and the lighter ones the $\hat{\mathbf{d}}$ vector. Both vectors are limited to the plane perpendicular to the large static magnetic field $\mathbf{B}_0$.

$$U_\perp \quad = \quad 1 - 2\hat{l}_z^2 - (\hat{\mathbf{l}} \times \hat{\mathbf{d}}_0)_z^2 - \frac{K_6}{\lambda_{\mathrm{d}}}(\boldsymbol{\nabla}\theta)^2 - \frac{K_5 - K_6}{\lambda_{\mathrm{d}}}(\hat{\mathbf{l}} \cdot \boldsymbol{\nabla}\theta)^2. \quad (19)$$

The resonance frequencies $\omega_{\parallel,k}$ and $\omega_{\perp,k}$ are related to the eigenvalues by

$$\omega_{\parallel,k}^2 \quad = \quad \Omega^2 \alpha_{\parallel,k} \quad (20)$$
$$\omega_{\perp,k}^2 \quad = \quad \omega_0^2 + \Omega^2 \alpha_{\perp,k}, \quad (21)$$

where $\Omega^2 = \mu_0 \gamma^2 \lambda_{\mathrm{d}}/\chi$ is the longitudinal resonance frequency in the A phase. Here χ is the susceptibility in the normal state and μ_0 is the vacuum permeability. Often the notation $R_{\perp,\parallel}^2$ is used instead of parameters $\alpha_{\perp,\parallel}$. In the bulk the lowest eigenvalues are given by $\alpha_{\parallel,\mathrm{b}} = \alpha_{\perp,\mathrm{b}} = 1$ and one may observe only the bulk peak in the absorption spectrum. In case of dipole unlocking also other eigenstates contribute to the power absorption. Typically there exists only one bound state with $\alpha < 1$. Since different textures usually give different locations for these satellite peaks, the absorption spectrum may be used as a tool to identify the textures. In Fig. 8 we have plotted the potential
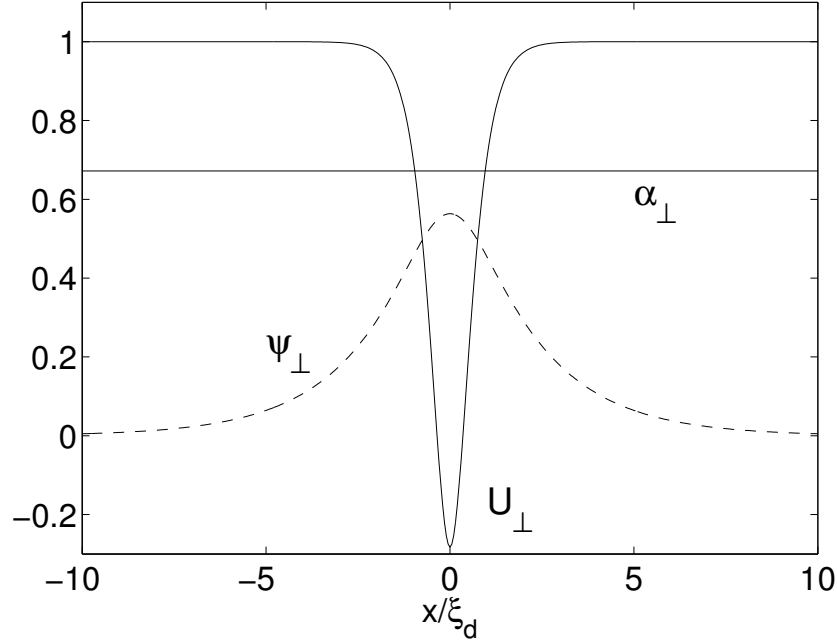
Figure 8: The lowest eigenstate for the transversal splay soliton at $T = T_c$. The dashed line is the wave function and the horizontal line the corresponding eigenvalue. The potential $U_\perp$ is given by the solid curve.

and the lowest eigenfunction together with the corresponding eigenvalue in the case of transversal splay soliton at $T = T_c$.

In publication [P3] we determine the location of the soliton satellite peak as a function of temperature. We also analyze the effect of the different parameters to the results. A good agreement with experiments [27–29] is usually achieved by using bare weak-coupling values for the hydrostatic parameters K_b, K_s *etc.* and using measurements by Greywall [30, 31] for the lowest Fermi-liquid parameters F_1^s and F_1^a. The higher Fermi-liquid parameters were omitted in our analysis since they are typically unknown and usually make the analysis much more complicated. Especially the results obtained for the longitudinal twist soliton support the prediction by Serene and Rainer [32] that the deviation of the hydrostatic parameters from the weak coupling values is small. The only essential difference between the experiment and theory appears in case of transversal splay soliton. This difference cannot be explained by uncertainties in different parameters but some of it can be removed by taking into account dissipation, and especially spin diffusion which is described in the following section.

15

3.2 Dissipation

When we include dissipation the absorption spectrum is no longer a set of delta peaks. In ^{3}He there are several processes that may cause line broadening. For transversal resonance, the inhomogeneity of the static magnetic field causes the Larmor frequency and therefore also the resonance frequency to depend on the location. This location dependence may also result from the nonuniform texture. Another reason for the line broadening is the nonequilibrium between normal and superfluid magnetizations, *i.e.*, the so-called Leggett-Takagi relaxation, which appears even in homogeneous superfluid ^{3}He [26, 33].

In publication [P3] we consider both the normal-superfluid relaxation and spin diffusion which only exists in the presence of nonuniform textures. These two mechanisms should be the main sources of dissipation in the A phase near T_c when the magnetic field is homogeneous. In the analysis we omit a very small temperature region below T_c, the so-called gapless region, where the orbital relaxation dominates the spin diffusion [34].

Calculations in publication [P3] are based on theory developed by Leggett and Takagi [26], where the spin polarization $\mathbf{S} = \mathbf{S}_p + \mathbf{S}_q$ consists of a superfluid (pair) part $\mathbf{S}_p$ and a normal (quasiparticle) part $\mathbf{S}_q$. Spin diffusion is taken into account by simply adding a term $\kappa \nabla^2 \mathbf{S}_q$ into the equation of motion for $\dot{\mathbf{S}}_q$ (see below). The tensor nature for the spin diffusion coefficient κ is omitted for simplicity. This should be appropriate at least for temperatures near T_c [5]. The equations of motions are

$$\dot{\mathbf{S}}_q = \gamma \mathbf{S}_q \times \left(\mathbf{B} - \mu_0 \gamma \frac{F_0^a}{\chi_0} \mathbf{S}_p \right) + \frac{1}{\tau} \left[(1-\lambda)\mathbf{S}_p - \lambda \mathbf{S}_q \right] + \kappa \nabla^2 \mathbf{S}_q \quad (22)$$

$$\dot{\mathbf{S}}_p = \gamma \mathbf{S}_p \times \left(\mathbf{B} - \mu_0 \gamma \frac{F_0^a}{\chi_0} \mathbf{S}_q \right) - \frac{1}{\tau} \left[(1-\lambda)\mathbf{S}_p - \lambda \mathbf{S}_q \right] - \hat{\mathbf{d}} \times \frac{\delta f}{\delta \hat{\mathbf{d}}} \quad (23)$$

$$\dot{\hat{\mathbf{d}}} = \gamma \hat{\mathbf{d}} \times \left[\mathbf{B} - \mu_0 \gamma \frac{F_0^a}{\chi_0} \mathbf{S}_q - \mu_0 \gamma \left(\frac{F_0^a}{\chi_0} + \frac{1}{\lambda \chi_0} \right) \mathbf{S}_p \right]. \quad (24)$$

Above χ_0 is the susceptibility in the absence of Fermi-liquid effects so that $\chi/\chi_0 = 1/(1 + F_0^a)$, where χ is the susceptibility in the normal state. Additionally $f = f_d + f_g$ contains the dipole and gradient terms in the hydrostatic energy density, defined by Eqs. (6) and (8) in the previous section. The function $\lambda(T/T_c)$ is defined as the equilibrium fraction of the superfluid magnetization. Compared to the dissipationless case we now have two more time scales appearing in the theory. One is the Leggett-Takagi relaxation time τ which describes the relaxation of $\mathbf{S}_p$ and $\mathbf{S}_q$ to they equilibrium values. The other is the spin diffusion time τ_D that is related to the spin-diffusion

16

coefficient κ by [35]

$$\kappa = \frac{1}{3}v_{\mathrm{F}}^2(1 + F_0^{\mathrm{a}})\tau_{\mathrm{D}}, \tag{25}$$

where v_{F} is the Fermi velocity. In our calculations this relation is used also in the superfluid state, even if it is actually derived for the normal state.

The Leggett-Takagi relaxation time τ can also be deduced from the linewidth of the bulk peak. In publication [P3] we used the value $\tau = 0.22 \times 10^{-6}T^{-2}$ s mK^2 that is measured for the normal state by Wheatley [3] but differs only slightly from measurements by Gully $et~al.$ [36] for the superfluid state. For the spin diffusion time τ_{D} there exist no accurate calculations in the case of the A phase, but the magnitude in the normal state should be of the same order as τ [37] and therefore we chose $\tau_{\mathrm{D}} = \tau$. The relative effect of these two dissipation mechanisms was analyzed by setting $\tau_{\mathrm{D}} = 0$ or $\tau = 0$ separately.

If we limit to linear deviations of $\hat{\mathbf{d}}$, $\mathbf{S}_{\mathrm{p}}$ and $\mathbf{S}_{\mathrm{q}}$ from their equilibrium values and assume a soliton structure, where $l_z = 0$, we obtain a linear matrix eigenvalue problem of the form (see publication [P3] for details)

$$A\psi = \omega\psi \tag{26}$$

for both longitudinal and transversal oscillations. The matrix A is obtained from the soliton texture at discretized points and contains now the two new timescales τ and τ_{D}. This eigenvalue problem is solved using standard library routines and the power absorption spectrum is calculated from the resulting eigenvectors ψ as described in publication [P3].

The only effect of the normal-superfluid relaxation seems to be line broadening, also in the presence of the soliton. For the longitudinal resonance the linewidth does not depend on magnetic field, but for the transversal case the width is inversely proportional to the field. Note that this analysis is valid when we consider the spectrum in the reduced frequencies $\alpha_\perp$ defined by Eq. (21). Line broadening is not the only effect of spin diffusion. It also shifts the resonance frequencies up. This can be seen especially in the transversal case where the effective diffusion coefficient depends linearly on the magnetic field. For that reason the effect for typical fields (about 5 mT) is about ten times larger than for longitudinal resonance, where no such field dependence exists. The spin diffusion can partly explain the differences between theory and experiment for the transversal splay soliton at temperatures near T_{c}. In that case the experimental points lie above the theoretical line calculated in the absence of dissipation. However, the calculated temperature dependence is too strong. The experimental dependence on the magnetic field, on the other hand, is not reported in any of the publications.

4   Impurities in ^{3}He

4.1   Quasiclassical approach

Since ^{3}He is naturally an ultra-pure liquid and its p-wave pairing state is well understood, it is an ideal material for studying the effects of impurities on unconventionally paired systems. As an impurity one uses porous silica-aerogel where typically 98%. . . 99.5% of the volume is empty. A sample photo on aerogel is illustrated in Fig. 9. When filled with helium the aerogel strands act as an impurity and scatter the helium quasiparticles. The average mean free path of a quasiparticle in aerogel is estimated to be around 200 nm, depending on the aerogel density. Impurity scattering results in a suppression of the superfluid state [38]. For example, the critical temperature T_c, pair amplitude Δ and superfluid density ρ_s are smaller than those in bulk. Quasiclassical theory is a natural choice when one wants to examine the effects of the impurities on ^{3}He.
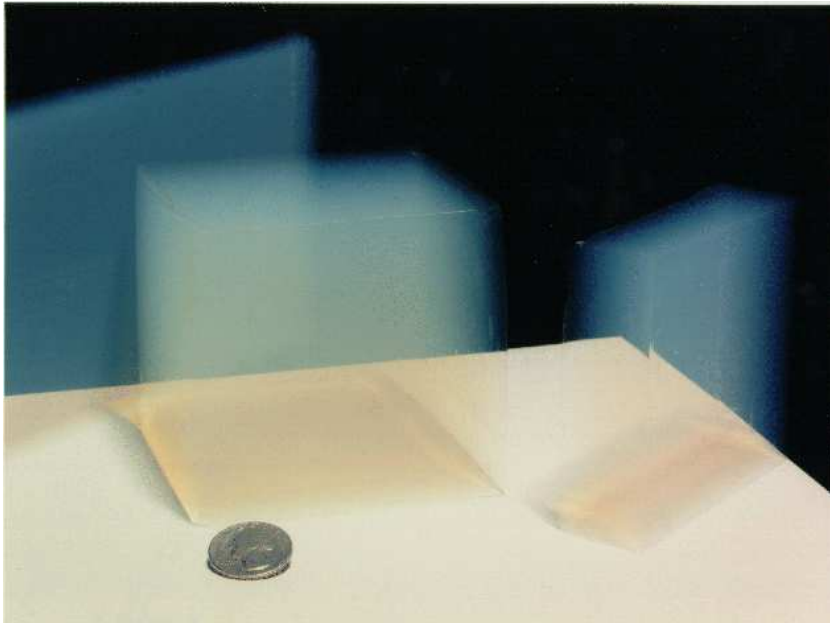

Figure 9: Photograph of aerogel samples (Photo courtesy of JPL Photolab and Robert Brown).

Originally the quasiclassical theory was developed for superconductors, but in its general form it can also be applied to other degenerate fermion systems, for example to ^{3}He and to neutron stars. The formulation presented

below is based on the article by Serene and Rainer [39]. The main assumption in the theory, required for the degeneracy, is that the temperature is much smaller than the Fermi temperature ($k_{\mathrm{B}}T \ll E_{\mathrm{F}}$). This is well satisfied in superfluid ^{3}He where the Fermi temperature $T_{\mathrm{F}} = E_{\mathrm{F}}/k_{\mathrm{B}} \approx 1$K. In its basic form the theory is only applicable when the characteristic length scales are much larger than the Fermi wavelength $\lambda_{\mathrm{F}} = 2\pi/k_{\mathrm{F}}$. In superfluid ^{3}He, the characteristic length is the coherence length that is defined by

$$\xi_0 = \hbar v_{\mathrm{F}}/2\pi k_{\mathrm{B}}T_{\mathrm{c}0}, \tag{27}$$

where $T_{\mathrm{c}0}$ is the transition temperature in pure helium and v_{F} is the Fermi velocity. Depending on the pressures, ξ_0 varies between 16 nm and 77 nm but is always much larger than the Fermi wave length $\lambda_{\mathrm{F}} \approx 0.7$ nm.

In quasiclassical theory one does not consider strongly interacting helium atoms, but weakly interacting quasiparticles with an effective mass m^*. This is 3 to 6 times larger than the mass m_3 of a ^{3}He atom. Since the mean free path of quasiparticles in pure helium is more than 1 μm, we may assume that the quasiparticles scatter mainly from aerogel strands and work in the weak coupling limit where quasiparticle-quasiparticle scattering is neglected.

Quasiclassical theory is formulated using a complex-valued 4×4 matrix Green's function or propagator $\breve{g}(\hat{\mathbf{k}}, \mathbf{r}, \epsilon_m)$. In equilibrium the arguments are the direction of the quasiparticle momentum $\hat{\mathbf{k}}$, position $\mathbf{r}$, and the Matsubara frequency $\epsilon_m = \pi k_{\mathrm{B}}T(2m - 1)$, where m is an integer. The propagator is represented as

$$\breve{g} = \begin{pmatrix} g + \mathbf{g} \cdot \boldsymbol{\sigma} & (f + \mathbf{f} \cdot \boldsymbol{\sigma})\mathrm{i}\underline{\sigma}_2 \\ \mathrm{i}\underline{\sigma}_2(\tilde{f} + \tilde{\mathbf{f}} \cdot \boldsymbol{\sigma}) & \tilde{g} - \underline{\sigma}_2\tilde{\mathbf{g}} \cdot \boldsymbol{\sigma}\,\underline{\sigma}_2 \end{pmatrix}. \tag{28}$$

where $\underline{\sigma}_i$:s are the 2×2 Pauli spin matrices and we have omitted the 2×2 identity matrices $\underline{1}$, for example, in front of f. The propagator satisfies the Eilenberger equation and the normalization condition:

$$\begin{aligned} [\mathrm{i}\epsilon_m\breve{\tau}_3 - \breve{\sigma}, \breve{g}] + \mathrm{i}\hbar v_{\mathrm{F}}\hat{\mathbf{k}} \cdot \nabla_{\mathbf{r}}\breve{g} &= 0 \\ \breve{g}\breve{g} &= -1, \end{aligned} \tag{29}$$

where $[A, B] = AB - BA$ denotes a commutator, and $\breve{\tau}_i$ denote Pauli matrices in the Nambu space; $\breve{\tau}_i = \underline{\sigma}_i \otimes \underline{1}$. Here the self energy matrix $\breve{\sigma} = \breve{\sigma}_{\mathrm{mf}} + \breve{\sigma}_{\mathrm{imp}}$ consists of mean field and impurity contributions. For ^{3}He, where we have spin-triplet pairing, the mean field part has the form

$$\breve{\sigma}_{\mathrm{mf}}(\hat{\mathbf{k}}, \mathbf{r}) = \begin{pmatrix} \nu(\hat{\mathbf{k}}, \mathbf{r}) + \boldsymbol{\nu}(\hat{\mathbf{k}}, \mathbf{r}) \cdot \boldsymbol{\sigma} & \boldsymbol{\Delta}(\hat{\mathbf{k}}, \mathbf{r}) \cdot \boldsymbol{\sigma}\mathrm{i}\underline{\sigma}_2 \\ \mathrm{i}\underline{\sigma}_2\boldsymbol{\Delta}^*(\hat{\mathbf{k}}, \mathbf{r}) \cdot \boldsymbol{\sigma} & \nu(-\hat{\mathbf{k}}, \mathbf{r}) - \underline{\sigma}_2\boldsymbol{\nu}(-\hat{\mathbf{k}}, \mathbf{r}) \cdot \boldsymbol{\sigma}\,\underline{\sigma}_2 \end{pmatrix}. \tag{30}$$

Here $\mathbf{\Delta}$ in the off-diagonal part is related to the order parameter $A_{\mu i}$ by $\Delta_\mu = A_{\mu i} \hat{k}_i$ and is determined by the self-consistency equation

$$\mathbf{\Delta}(\hat{\mathbf{k}}, \mathbf{r}) \ln \frac{T}{T_{c0}} + \pi k_{\mathrm{B}} T \sum_{\epsilon_m} \left[\frac{\mathbf{\Delta}(\hat{\mathbf{k}}, \mathbf{r})}{|\epsilon_m|} - 3 \left\langle (\hat{\mathbf{k}} \cdot \hat{\mathbf{k}}') \mathbf{f}(\hat{\mathbf{k}}', \mathbf{r}, \epsilon_m) \right\rangle_{\hat{\mathbf{k}}'} \right] = 0, \quad (31)$$

where $\langle \ldots \rangle_{\hat{\mathbf{k}}}$ denotes the angular average with respect to direction $\hat{\mathbf{k}}$. In the diagonal part the real-valued functions ν and $\boldsymbol{\nu}$ are given by

$$\nu(\hat{\mathbf{k}}, \mathbf{r}) = \pi k_{\mathrm{B}} T \sum_{\epsilon_m} \left\langle A^s(\hat{\mathbf{k}} \cdot \hat{\mathbf{k}}') g(\hat{\mathbf{k}}', \mathbf{r}, \epsilon_m) \right\rangle_{\hat{\mathbf{k}}'}$$

$$\boldsymbol{\nu}(\hat{\mathbf{k}}, \mathbf{r}) = \pi k_{\mathrm{B}} T \sum_{\epsilon_m} \left\langle A^a(\hat{\mathbf{k}} \cdot \hat{\mathbf{k}}') \mathbf{g}(\hat{\mathbf{k}}', \mathbf{r}, \epsilon_m) \right\rangle_{\hat{\mathbf{k}}'} \quad (32)$$

and the functions $A^{s,a}(x)$ may be expressed using Legendre polynomials $P_l(x)$ and Fermi liquid parameters $F_l^{s,a}$ by

$$A^{s,a}(x) = \sum_{l=0}^{\infty} \frac{F_l^{s,a}}{1 + \frac{1}{2l+1} F_l^{s,a}} P_l(x). \quad (33)$$

In the presence of impurities we must take into account the impurity self energy $\breve{\sigma}_{\mathrm{imp}}$. It is related to the forward-scattering t-matrix by [40]

$$\breve{\sigma}_{\mathrm{imp}}(\hat{\mathbf{k}}, \mathbf{r}, \epsilon_m) = n(\mathbf{r}) \breve{t}(\hat{\mathbf{k}}, \hat{\mathbf{k}}, \mathbf{r}, \epsilon_m), \quad (34)$$

where $n(\mathbf{r})$ is the impurity density. Normally this formula is applied for constant n, but it should also be valid more generally if the impurity positions are allowed to be uncertain on the scale of the Fermi wave length. The t-matrix obeys the following integral equation

$$\breve{t}(\hat{\mathbf{k}}, \hat{\mathbf{k}}', \mathbf{r}, \epsilon_m) = \breve{v}(\hat{\mathbf{k}}, \hat{\mathbf{k}}') + \pi N_F \left\langle \breve{v}(\hat{\mathbf{k}}, \hat{\mathbf{k}}'') \breve{g}(\hat{\mathbf{k}}'', \mathbf{r}, \epsilon_m) \breve{t}(\hat{\mathbf{k}}'', \hat{\mathbf{k}}', \mathbf{r}, \epsilon_m) \right\rangle_{\hat{\mathbf{k}}''}. \quad (35)$$

where $2N_{\mathrm{F}} = m^* k_{\mathrm{F}} / \pi^2 \hbar^2$ is the total density of states on the Fermi surface and the effective mass m^* is obtained from $m^*/m_3 = 1 + F_1^s/3$. The matrix $\breve{v}$ is related to the scattering potential and for non-magnetic scattering $\breve{v} = v \breve{1}$, where a spherically symmetric potential v may be written as

$$v(\hat{\mathbf{k}}, \hat{\mathbf{k}}') = \sum_{l=0}^{\infty} \frac{2l+1}{4\pi} v_l P_l(\hat{\mathbf{k}} \cdot \hat{\mathbf{k}}'). \quad (36)$$

The partial wave expansion coefficients, v_l:s, are related to the scattering phase shifts δ_l by $v_l = -(4/N_{\mathrm{F}}) \tan \delta_l$. The quasiparticle mean free path is

$\ell = (n\sigma)^{-1}$ [41], where the normal-state transport cross section σ is given by the scattering phase shifts as [42]

$$\sigma = \frac{4\pi}{k_{\mathrm{F}}^2} \sum_{l=0}^{\infty} (l+1) \sin^2(\delta_{l+1} - \delta_l). \tag{37}$$

Within quasiclassical theory the mass supercurrent density is given by

$$\mathbf{j}_{\mathrm{s}}(\mathbf{r}) = 2\pi m v_{\mathrm{F}} N_{\mathrm{F}} k_{\mathrm{B}} T \sum_{\epsilon_m} \left\langle \hat{\mathbf{k}} g(\hat{\mathbf{k}}, \mathbf{r}, \epsilon_m) \right\rangle_{\hat{\mathbf{k}}}, \tag{38}$$

where g is obtained from the definition of the propagator in Eq. (28). This is also the total flow, since we chose our coordinates such that $v_{\mathrm{n}} = 0$.

If one attempts to apply the quasiclassical theory of ^{3}He to real aerogel samples with quite complex structures, one soon notices that the task is, if not impossible, at least numerically too demanding. One should therefore try to extract only the essential features from the aerogel structure and calculate the experimentally measurable quantities using some simplified model. In the following sections we describe two simple scattering models and their numerical implementations that were used in publications [P4], [P5] and [P6].

4.2 Homogeneous Scattering Model

In publication [P4] we consider the homogeneous scattering model (HSM), where the impurity density n is assumed constant. This is a standard model used for impurities in metals and results from averaging over the impurity locations [40]. The scattering is assumed to be isotropic and non-magnetic. This model has been applied extensively on superconductors but also on ^{3}He [43–54].

For homogeneous scattering the form of the order parameter in both phases can be assumed to remain unchanged from the bulk forms [given by Eqs. (1) and (2)]. Only the amplitude of the pairing potential Δ is modified due to impurities. For zero superfluid velocity all the position dependence drops out and the solution may be obtained by choosing $\nu = 0$, $\boldsymbol{\nu} = 0$ and taking

$$\breve{\sigma}_{\mathrm{imp}}(\hat{\mathbf{k}}, \epsilon_m) = a(\epsilon_m)\breve{1} + b(\epsilon_m)\breve{\tau}_3 + c(\epsilon_m)\breve{\Delta}(\hat{\mathbf{k}}), \tag{39}$$

where $\breve{\Delta}$ denotes the off-diagonal part in $\breve{\sigma}_{\mathrm{mf}}$. When we consider only s-wave scattering we may set $c = 0$. The Eilenberger equation and the normalization condition now imply that the propagator has the same form as in bulk, namely

$$\breve{g} = \frac{-\mathrm{i}(\epsilon_m - b)\breve{\tau}_3 + (1+c)\breve{\Delta}}{\sqrt{(\epsilon_m - b)^2 + (1+c)^2|\boldsymbol{\Delta}|^2}}. \tag{40}$$

21

The numerical solution now reduces to finding $b(\epsilon_m)$, $c(\epsilon_m)$ and Δ using the t-matrix equation (35) and the gap-equation (31). Parameters $a(\epsilon_m)$ are of no interest since they drop out and do not affect the quantities that we are interested in. The numerical method is based on Newton iteration where the equation $F(x) = 0$ is solved iteratively by

$$x_{n+1} = x_n - F(x_n)/F'(x_n). \tag{41}$$

The precise equations solved can be found in publication [P4]. In order to avoid complicated angular integrals, the effect of the higher partial waves was only taken into account for the pair amplitude Δ in the B phase. In the A phase we limited to the s-wave scattering. For accurate results the number of required Matsubara frequencies depends essentially on temperature and becomes quite large at low temperatures. This is not a problem for the HSM with the current computers, but may cause difficulties with more complicated models as described below.

In case of the superfluid density defined by $\rho_s = \lim_{v_s \to 0} j_s/v_s$, we limit to the s-wave scattering in both phases. We make a gradient expansion $\breve{g} = \breve{g}_0 + \breve{g}_1 + \ldots$ for the propagator, where $\breve{g}_0(\hat{\mathbf{k}}, \mathbf{r}, \epsilon_m)$ is the solution above [given by Eq. (40)], but with the order parameter $\boldsymbol{\Delta}(\hat{\mathbf{k}}, \mathbf{r}) = \exp(i\mathbf{q} \cdot \mathbf{r})\boldsymbol{\Delta}(\hat{\mathbf{k}})$. This corresponds to a superfluid velocity $\mathbf{v}_s = \frac{\hbar}{2m_3}\mathbf{q}$. The first-order correction $\breve{g}_1$ is linear in $\nabla_{\mathbf{r}}\breve{g}_0$ and can, after some algebra, be expressed using the values $b(\epsilon_m)$ and Δ calculated above. After this one may calculate the mass current using Eq. (38) and the superfluid density from the above definition.

In the B phase ρ_s is simply a scalar but for the A phase there exist two eigenvalues ($\rho_\perp$ and $\rho_\parallel$) for the superfluid density depending on the direction of the superfluid velocity relative to anisotropy axis $\hat{\mathbf{l}}$. For the pairing amplitude there is no pressure dependence in the weak-coupling approximation, and from the superfluid density the pressure dependence can be removed by defining a pressure-independent bare superfluid density ρ_s^b as

$$\frac{\rho_s^b}{\rho_{\text{tot}}} = \frac{\left(1 + \frac{1}{3}F_1^s\right)(\rho_s/\rho_{\text{tot}})}{1 + \frac{1}{3}F_1^s(\rho_s/\rho_{\text{tot}})}, \tag{42}$$

where ρ_{tot} is the total density of the fluid. This is exact for the B phase, but for the A phase, where similar equations exist for $\rho_\perp$ and $\rho_\parallel$, the relation is valid only when ignoring the F_l^s terms with $l > 2$. Since the aerogel structure contains random strands, the $\hat{\mathbf{l}}$ vector is most likely also oriented quite randomly. Therefore, for the A phase, the experimentally measured value for the superfluid density is an average over all directions, and given by $\rho_{\text{ave}} = (2\rho_\perp + \rho_\parallel)/3$.

Due to the impurities, the superfluid transition temperature T_c, which in the weak coupling limit is same for both phases, is suppressed relative to the T_{c0} for a clean system. The ratio T_c/T_{c0} depends only on the value ξ_0/ℓ through the condition

$$\ln \frac{T_c}{T_{c0}} + 2\pi k_B T_c \sum_{\epsilon_m > 0} \left(\frac{1}{\epsilon_m} - \frac{1}{\epsilon_m + \hbar v_F/2\ell} \right). \qquad (43)$$

This suppression is plotted for example in Fig. 4 of publication [P6]. The superfluidity becomes completely suppressed when $\xi_0/\ell = 0.28$.

The suppression of the pair amplitude Δ and the (bare) superfluid density is analyzed in [P4] in detail. When considering the B-phase pairing potential one already notices that all the essential features are captured when limiting to s-wave scattering with $\sin^2 \delta_0 = 0.5$. The behavior of the suppression is very similar in both phases also for the superfluid density. When comparing the results with experiments the mean free path ℓ should be considered almost pressure independent, since the structure of aerogel is almost pressure independent and also the Fermi wave vector k_F depends only slightly on pressure. The critical temperatures can be fitted fairly well with experiments [38, 55–59], simply by choosing a suitable mean free path for the each aerogel sample. Only at lower pressures, where ξ_0 is largest, the fit becomes somewhat poorer. For the pair amplitude and superfluid density, the measured values [55–58, 60] are much smaller than predicted by the homogeneous scattering model. The differences are too large to be explained by different scattering parameters that appear in the model. These differences can be partly explained by taking into account that the scattering is inhomogeneous. The model for inhomogeneous scattering is described in the following section.

4.3 Isotropic Inhomogeneous Scattering Model

Since the homogeneous scattering model seems to be insufficient to explain the experimentally measured critical temperatures and superfluid densities, some other model should be considered. A natural way to explain the differences between theory and experiments is to take into account that the scattering is inhomogeneous. The isotropic inhomogeneous scattering model (IISM) allows the impurity distribution to vary in space but at the same time keeps the medium uniform and isotropic on a large scale [43].

In the IISM the impurity density is assumed to form a periodic lattice where the unit cell can be approximated by a sphere with radius R. This assumption is equivalent to using a spherical cell approximation for a Wigner-Seitz unit cell in solid state physics [61]. Inside the spherical unit cell the
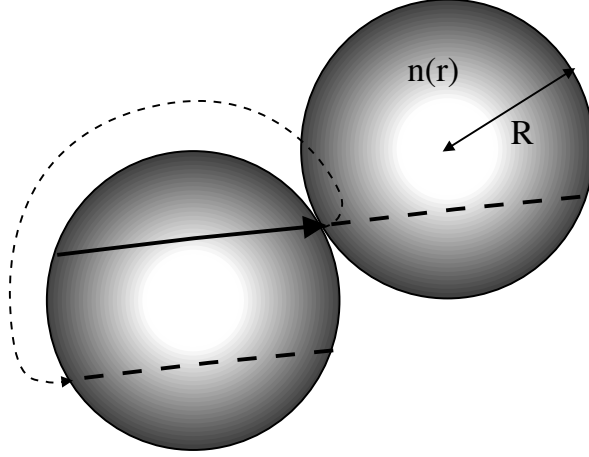
Figure 10: Sphere used to approximate the unit cell in the IISM. The shading intensity denotes the impurity density $n(r)$ and the dashed lines illustrate the boundary condition where a quasiparticle exiting the sphere is equivalent to another quasiparticle entering at the opposite point.

impurity density n is allowed to depend only on the radial coordinate r. The boundary conditions may be chosen such that a quasiparticle exiting the sphere is returned to the diametrically opposite point without changing its momentum or spin, as illustrated in Fig. 10. For nonzero superfluid velocity $\mathbf{v}_\mathrm{s} = \frac{\hbar}{2m_3}\mathbf{q}$, which is well defined only on scales larger than R, the order parameter is no longer strictly periodic in the lattice but has the Bloch form $A_{\mu j}(\mathbf{r}) = A_{\mu j}^0(\mathbf{r}) \exp(i\mathbf{r} \cdot \mathbf{q})$, where $A_{\mu j}^0(\mathbf{r})$ has the periodicity of the lattice. This extra phase shift can be expressed using the Green's function as

$$\breve{g}(\hat{\mathbf{k}}, R\hat{\mathbf{r}}, \epsilon_m) = \exp\left(i\mathbf{q} \cdot R\hat{\mathbf{r}} \, \breve{\tau}_3\right) \breve{g}(\hat{\mathbf{k}}, -R\hat{\mathbf{r}}, \epsilon_m) \exp\left(-i\mathbf{q} \cdot R\hat{\mathbf{r}} \, \breve{\tau}_3\right). \qquad (44)$$

Since the scattering is now inhomogeneous, the A-phase or the B-phase forms for the order parameter must be modified. However, no essentially new phases are expected to appear [43]. Based on the symmetry arguments the B phase order parameter for $\mathbf{v}_\mathrm{s} = 0$ can be deduced to take the form

$$\overleftrightarrow{A}(r, \phi, \theta) = e^{i\chi}\overleftrightarrow{R}\left[\Delta_r(r)\hat{\mathbf{r}}\hat{\mathbf{r}} + \Delta_a(r)(\hat{\boldsymbol{\theta}}\hat{\boldsymbol{\theta}} + \hat{\boldsymbol{\phi}}\hat{\boldsymbol{\phi}})\right], \qquad (45)$$

in the spherical coordinates (r, ϕ, θ). Here the phase χ and the rotation matrix $\overleftrightarrow{R}$ are arbitrary constants and the amplitudes $\Delta_r(r)$ and $\Delta_a(r)$ are real and functions of r only. For the A-type phase the order parameter is more complicated due to anisotropy. If we choose the cylindrical coordinates

(ρ, ϕ, z) such that z is along the anisotropy axis $\hat{\mathbf{l}}$, then the order parameter for zero superfluid velocity can be written as

$$\overset{\leftrightarrow}{A}(\rho, \phi, z) = e^{\mathrm{i}\phi}\hat{\mathbf{d}}\left[\Delta_\rho(\rho, z)\hat{\boldsymbol{\rho}} + \mathrm{i}\Delta_\phi(\rho, z)\hat{\boldsymbol{\phi}} + \Delta_z(\rho, z)\hat{\mathbf{z}}\right]. \tag{46}$$

Here $\hat{\mathbf{d}}$ is an arbitrary constant unit vector and the amplitudes Δ_i are real and depend on ρ and z. For nonzero superfluid velocity in the z-direction the calculations are limited to the B-type phase where the order parameter may be written as

$$\overset{\leftrightarrow}{A}(\rho, \phi, z) = e^{\mathrm{i}\chi}\overset{\leftrightarrow}{R}\left[\Delta_{\rho\rho}\hat{\boldsymbol{\rho}}\hat{\boldsymbol{\rho}} + \Delta_{\phi\phi}\hat{\boldsymbol{\phi}}\hat{\boldsymbol{\phi}} + \Delta_{zz}\hat{\mathbf{z}}\hat{\mathbf{z}} + \Delta_{\rho z}\hat{\boldsymbol{\rho}}\hat{\mathbf{z}} + \Delta_{z\rho}\hat{\mathbf{z}}\hat{\boldsymbol{\rho}}\right]. \tag{47}$$

Now the terms $\Delta_{\mu i}$ are complex and depend on ρ and z. Inside the sphere the superfluid mass current $\mathbf{j}_{\mathrm{s}}(\mathbf{r})$ has non-zero ρ and z components. The experimentally measured value, which is an average of these over the sphere, has only the z component left.

In order to keep the calculations simple we limit to s-wave scattering and take into account only the lowest Fermi-liquid parameters. Limiting to s-wave scattering only may sound too restrictive since even in the simplest hard-sphere approximation for the impurity, most of the scattering takes place via higher partial waves. However, as noted already in the HSM, most of the essential features are captured using only s-wave scattering with random phase shifts δ_0 (*i.e.*, essentially by using $\sin^2\delta_0 = 0.5$).

For the impurity density $n(r)$ we used two different types of profiles. In the first profile the impurity is concentrated near the shell of the sphere. This type of *void* profile can be considered to form a self-supporting structure but at the same time it forces the flow through the regions with high impurity density. In the other profile the impurity is concentrated at the center of the sphere. This *cluster* type profile allows the flow to go through the low-impurity regions, but at the same time there exist trajectories near the shell with very large mean free paths due to the periodic boundaries. In real aerogel with quite randomly oriented strands, the scattering effect on quasiparticles is probably somewhere between these two extremes.

4.4   IISM and numerics

The numerical solution for solving the Eilenberger equation is based on the so-called "multiplication trick" [62]. This trick makes use of the fact that the product of two solutions is also a solution of the Eilenberger equation. When using another parametrization for the propagator (see for example Ref. [62]) the Eilenberger equation separates into three disjoint sets of equations. One

of these sets contains the correct physical solution that satisfies the symmetry $\breve{g} = -\breve{\tau}_2 \breve{g} \breve{\tau}_2$ that is valid in the absence of the magnetic field. It is difficult to find this correct physical solution by direct numerical integration of the Eilenberger equation due to an instability towards one of the two exponential unphysical solutions. Fortunately, the correct physical solution can be obtained as a commutator

$$\breve{g} = \frac{\mathrm{i}[\breve{g}_\prec, \breve{g}_\succ]}{\{\breve{g}_\prec, \breve{g}_\succ\}}, \tag{48}$$

where $\breve{g}_\prec$ and $\breve{g}_\succ$ are the exponentially increasing and decreasing solutions of the second set that contains unphysical propagators with the symmetry $\breve{g} = +\breve{\tau}_2 \breve{g} \breve{\tau}_2$. They are normalized to zero ($\breve{g}_\succ \breve{g}_\prec = 0$) and have the form

$$\breve{g}_\succ = \begin{pmatrix} \mathbf{c}_\succ \cdot \boldsymbol{\sigma} & [a_\prec + b_\succ]\mathrm{i}\underline{\sigma}_2 \\ \mathrm{i}\underline{\sigma}_2[a_\prec - b_\prec] & -\underline{\sigma}_2 \mathbf{c}_\succ \cdot \boldsymbol{\sigma} \, \sigma_2 \end{pmatrix}. \tag{49}$$

The exponentially increasing solution along one trajectory is obtained by using the fourth order Runge-Kutta method. The decreasing solution is obtained from other symmetries instead of reversing the direction in the Runge-Kutta integration.

Since the Runge-Kutta integration is performed along some fixed trajectory direction one cannot work only in cylindrical/spherical coordinates but must also use cartesian "trajectory coordinates". Therefore in the numerical routine one frequently needs coordinate transformations between the trajectory coordinates and spherical/cylindrical coordinates.

The main goal for the routine is to find the values for the fields $A_{\mu i}$, $\breve{\sigma}_{\mathrm{imp}}$ and ν at discretized points (ρ_i, z_j) (or at r_i in case of B phase with no supercurrent) inside the sphere for a given impurity profile $n(r)$. At the beginning of the calculation some initial guess is taken for the fields everywhere and for the propagator at the beginning of the trajectory. Usually the exact results from the HSM were used for this. These values are then converted to the trajectory coordinates where the coordinate u is along the trajectory and the two others (b and t) specify the position of the trajectory inside the sphere. Next the Eilenberger equation is solved along the trajectory by using the multiplication trick described above. This is repeated for all Matsubara frequencies $|\epsilon_m| \leq \epsilon_{N_e}$ and for all trajectories that are specified by the coordinates b and t and the angle α between the trajectory and the z-axis. For the B phase without the current the symmetries are higher and only the coordinate b is needed to go through all the trajectories.

Next the propagator is converted back to the cylindrical/spherical coordinates. The required angular averages are calculated and the self-consistency equations are solved as described below. Now, with better estimates for

26

the fields, the iteration is restarted. When solving the Eilenberger equation again, the values for the exponential propagator at the previous step and the boundary condition (44) is used. The iteration loop is then repeated until convergence.

Typically only a few Matsubara frequencies are needed to obtain quite accurate results for temperatures near T_c. However, at lower temperatures the number of required frequencies increases. In order to reduce the number of frequencies, we combined the general quasiclassical equations with the equations from the Ginzburg-Landau (GL) theory that is valid for $|A_{\mu i}| \ll |\epsilon_m|$ [46]. The most important self-consistency equation is the gap equation (31) which now takes in cartesian coordinates the form

$$
A_{\mu i} \ln \frac{T}{T_{c0}} + \pi T k_B \sum_{|\epsilon_m| \leq \epsilon_{N_e}} \left[\frac{A_{\mu i}}{|\epsilon_m|} - 3 \int \frac{d^2\hat{\mathbf{k}}}{4\pi} f_\mu(\hat{\mathbf{k}}, \mathbf{r}, \epsilon_m) k_i \right] + \alpha A_{\mu i}
$$
$$
+ 2\beta_1 A_{\nu j} A_{\nu j} A_{\mu i}^* + 2\beta_2 A_{\nu j} A_{\nu j}^* A_{\mu i} + 2\beta_3 A_{\mu j} A_{\nu j} A_{\nu i}^* + 2\beta_4 A_{\mu j} A_{\nu j}^* A_{\nu i}
$$
$$
+ 2\beta_5 A_{\mu j}^* A_{\nu j} A_{\nu i} - K_2 \partial_j \partial_j A_{\mu i} - (K_1 + K_3) \partial_i \partial_j A_{\mu j} = 0. \quad (50)
$$

Here the summation over repeated indices is assumed. The term N_e is the number of positive Matsubara frequencies calculated exactly. Ginzburg-Landau approximation is achieved when $N_e = 0$. The parameters α, β_i and K_i are calculated in Refs. [43, 46] limiting to the s-wave scattering and neglecting any strong coupling effects. These parameters contain infinite sums that can be approximated using Euler-MacLaurin integral formulas

$$
\sum_{n=m_1}^{m_2-1} f(n + \frac{1}{2}) = \int_{m_1}^{m_2} ds f(s) + \frac{1}{24} [f'(m_1) - f'(m_2)] + O(f'''), \quad (51)
$$

where f' denotes the derivate. When applying this formula, for example for the parameter α, one finds that

$$
\alpha = \sum_{m=N_e+1}^{M} \frac{y}{(m - \frac{1}{2})(m - \frac{1}{2} + y)} + \ln(1 + \frac{y}{M}) - \frac{1}{24M^2} + \frac{1}{24(M + y)^2}. \quad (52)
$$

The term $y(\mathbf{r}) = \hbar v_F / 4\pi T \ell(\mathbf{r}) = \xi_0 T_{c0} / 2\ell(\mathbf{r}) T$ measures the local strength of the scattering. The upper limit M in the summation may be chosen to be of reasonable size since the error is of order $O(M^{-4})$, or less. The order parameter at each step is obtained from Eq. (50) simply by approximating the β_i- and K_i-terms by the values obtained in the previous step and solving the remaining linear equation for $A_{\mu i}$.

Since we were assuming a random phase shift δ_0, the impurity self-energy matrix $\breve{\sigma}_{\text{imp}}$ can be expressed simply using the angular averages of the propagator. Therefore one does not need to solve the t-matrix equation iteratively.

The high-energy corrections for the field ν can be obtained from the GL-form for the superfluid mass current. The current is given in cartesian coordinates by [5, 63]

$$
\begin{aligned}
j_{\mathrm{s},i} &= 2m_3 v_{\mathrm{F}} N_{\mathrm{F}} \left[\pi k_{\mathrm{B}} T \sum_{|\epsilon_m| \leq \epsilon_{N_e}} \int \frac{d^2\hat{\mathbf{k}}}{4\pi} k_i g(\hat{\mathbf{k}}, \mathbf{r}, \epsilon_m) \right. \\
&+ \left. \frac{2}{3\hbar v_{\mathrm{F}}} \mathrm{Im} \left(K_1 A_{\mu i}^* \partial_j A_{\mu j} + K_2 A_{\mu j}^* \partial_i A_{\mu j} + K_3 A_{\mu j}^* \partial_j A_{\mu i} \right) \right].
\end{aligned} \tag{53}
$$

and since we were ignoring the Fermi-liquid parameters higher than F_1^s, the field ν is simply given by

$$
\nu = \frac{1}{2m_3 v_{\mathrm{F}} N_{\mathrm{F}}} \frac{F_1^s}{1 + \frac{1}{3} F_1^s} \hat{\mathbf{k}} \cdot \mathbf{j}_{\mathrm{s}}. \tag{54}
$$

In experiments the measured values correspond to an average value inside the sphere used in the IISM. The superfluid density, for example, can be measured by folding a sample of aerogel around a vibrating wire and measuring the resonance frequency of the wire. The same method is used to determine the superfluid density in bulk helium, but without the aerogel sample. In publications [P5] and [P6] these average values are presented using different impurity profiles and with various cell radii. The results are compared with experiments [38, 55–60]. Even if no exact fit with experiment can be achieved, the results are much better than the ones obtained by using the homogeneous model. This is a strong indication that the scattering in aerogel is inhomogeneous.

5   Discussion

In the above introduction I have briefly described the hydrodynamic and quasiclassical theories which are commonly used to describe the behavior of superfluid ^{3}He. I have explained how the hydrodynamic theory was applied to determine the vortex texture at the A-B phase boundary, determine the NMR spectrum of solitons and the stability of the helical textures. The quasiclassical theory was used to analyze the effect of the impurities in superfluid ^{3}He.

As a result of the hydrodynamic calculations, two new interface vortex textures were found to appear at the A-B phase boundary. The stability analysis of the helical texture was extended to contain a wider parameter space than previously. The exact structure of the splay soliton was determined and the effect of dissipation on the absorbtion spectrum was calculated. For the two dissipation mechanisms considered, the normal-superfluid relaxation causes only line broadening, but the spin diffusion also shifts the soliton satellite peak to higher frequencies.

The effect of aerogel on superfluid ^{3}He was described by using both a homogeneous scattering model (HSM) and an isotropic inhomogeneous scattering model (IISM). Of these two the inhomogeneous model yields better correspondence with the experiments. This indicates that the scattering of helium quasiparticles from the aerogel strands is inhomogeneous.

The problems introduced in this thesis illustrate the richness of different phenomena present in superfluid ^{3}He. The relatively good agreement between theory and experiment indicate that the present theories are already well developed. Nowadays computers and numerical algorithms provide a powerful tool for solving a wide variety of previously unsolved problems.

References

[1] D. D. Osheroff, R. C. Richardson, and D. M. Lee, Phys. Rev. Lett. **28**, 885 (1972).

[2] G. E. Volovik, *Exotic Properties of Superfluid ^3He* (World Scientific, Singapore, 1992).

[3] J. C. Wheatley, Rev. Mod. Phys. **47**, 415 (1975).

[4] A. J. Leggett, Rev. Mod. Phys. **47**, 331 (1975).

[5] D. Vollhardt and P. Wölfle, *The Superfluid Phases of Helium 3* (Taylor and Francis, London, 1990).

[6] R. Balian and N. R. Werthamer, Phys. Rev. **131**, 1553 (1963).

[7] P. W. Anderson and W. F. Brinkman, Phys. Rev. Lett. **30**, 1108 (1973).

[8] E. V. Thuneberg, Phys. Rev. Lett. **56**, 359 (1986).

[9] M. M. Salomaa and G. E. Volovik, Phys. Rev. Lett. **51**, 2040 (1983).

[10] M. M. Salomaa and G. E. Volovik, Phys. Rev. B **31**, 203 (1985).

[11] A. L. Fetter, in *Progress in Low Temperature Physics*, edited by D. F. Brewer (Elsevier, Amsterdam, 1986), Vol. X, p. 1.

[12] M. M. Salomaa and G. E. Volovik, Rev. Mod. Phys. **59**, 533 (1987); Erratum: *ibid.* **60**, 573 (1988).

[13] M. C. Cross, J. Low Temp. Phys. **21**, 525 (1975).

[14] M. Dörfle, Phys. Rev. B **24**, 6336 (1981).

[15] J. R. Hook, in *Helium Three*, edited by W. P. Halperin and L. P. Pitaevskii (Elsevier, Amsterdam, 1990), p. 135.

[16] E. V. Thuneberg, J. Low Temp. Phys. **122**, 657 (2001).

[17] Ü. Parts, J. M. Karimäki, J. H. Koivuniemi, M. Krusius, V. M. H. Ruutu, E. V. Thuneberg, and G. E. Volovik, Phys. Rev. Lett. **75**, 3320 (1995).

[18] R. Blaauwgeers, V. B. Eltsov, G. Eska, A. P. Finne, R. P. Haley, M. Krusius, J. J. Ruohio, L. Skrbek, and G. E. Volovik, Phys. Rev. Lett. **89**, 155301 (2002).

[19] M. C. Cross, in *Quantum Fluids and Solids*, edited by S. B. Trickey, E. D. Adams, and J. W. Duffy (Plenum Press, New York, 1977), p. 183.

[20] R. Kaul and H. Kleinert, J. Low Temp. Phys **38**, 539 (1980).

[21] N. Schopohl, Phys. Rev. Lett. **58**, 1664 (1987).

[22] Y. R. Lin-Liu, D. Vollhardt, and K. Maki, Phys. Rev. B **20**, 159 (1979).

[23] K. Maki and P. Kumar, Phys. Rev. B **16**, 182 (1977).

[24] K. Maki and P. Kumar, Phys. Rev. B **17**, 1088 (1978).

[25] A. J. Leggett, Ann. Phys. **85**, 11 (1974).

[26] A. J. Leggett and S. Tagagi, Ann. Phys. **106**, 79 (1977).

[27] O. Avenel, M. E. Bernier, E. J. Varoquaux, and C. Vibet, in *Proceedings of the Fourteenth International Conference on Low Temperature Physics*, edited by M. Krusius and M. Vuorio (North-Holland, Amsterdam, 1975), Vol. 5, p. 429.

[28] C. M. Gould and D. M. Lee, Phys. Rev. Lett. **37**, 1223 (1976).

[29] C. M. Gould, T. J. Bartolac, and H. M. Bozler, J. Low Temp. Phys. **39**, 291 (1980).

[30] D. S. Greywall, Phys. Rev. B **33**, 7520 (1986).

[31] D. S. Greywall, Phys. Rev. B **27**, 2747 (1983).

[32] J. W. Serene and D. Rainer, Phys. Rev. B **17**, 2901 (1978).

[33] R. Combescot, Phys. Rev. B **13**, 126 (1976).

[34] A. J. Leggett and S. Takagi, Ann. Phys. **110**, 353 (1978).

[35] A. J. Leggett, J. Phys. C **3**, 448 (1970).

[36] W. J. Gully, C. M. Gould, R. C. Richardson, and D. M. Lee, J. Low Temp. Phys. **24**, 563 (1976).

[37] A. S. Sachrajda, D. F. Brewer, and W. S. Truscott, J. Low Temp. Phys. **56**, 617 (1984).

[38] J. V. Porto and J. M. Parpia, Phys. Rev. Lett. **74**, 4667 (1995).

[39] J. W. Serene and D. Rainer, Phys. Rep. **101**, 221 (1983).

[40] A. A. Abrikosov, L. P. Gorkov, and I. E. Dzyaloshinski, *Methods of Quantum Field Theory in Statistical Physics* (Prentice Hall, Englewood Cliffs, N. J., 1963).

[41] E. Merzbacher, *Quantum Mechanics* (Wiley, New York, 1961).

[42] G. Baym, C. J. Pethick, and M. Salomaa, J. Low Temp. Phys **36**, 431 (1979).

[43] E. V. Thuneberg, S. K. Yip, M. Fogelström, and J. A. Sauls, Phys. Rev. Lett. **80**, 2861 (1998).

[44] G. Baramidze, G. Kharadze, and G. Vachnadze, Pisma Zh. Éksp. Teor. Fiz. **63**, 95 (1996), [JETP Lett. **63**, 107 (1996)].

[45] V. P. Mineev, Pis'ma Zh. Éksp. Teor. Fiz. **66**, 655 (1997), [JETP Lett. **66**, 693 (1997)].

[46] E. V. Thuneberg, in *Quasiclassical methods in superconductivity and superfluidity, Verditz 96*, edited by D. Rainer and J. A. Sauls (1998), p. 53. (cond-mat/9802044).

[47] D. Rainer and J. A. Sauls, J. Low. Temp. Phys. **110**, 525 (1998).

[48] G. Baramidze and G. Kharadze, J. Exp. Theor. Fiz. **115**, 754 (1999), [J. Exp. Theor. Phys. **88**, 415 (1999)].

[49] S. Higashitani, J. Low Temp. Phys. **114**, 161 (1999).

[50] P. Sharma and J. A. Sauls, J. Low Temp. Phys. **125**, 115 (2001).

[51] V. P. Mineev and P. L. Krotkov, Phys. Rev. B **65**, 024501 (2002).

[52] G. Baramidze and G. Kharadze, J. Phys.: Condens. Matter **14**, 7471 (2002).

[53] P. Sharma and J. A. Sauls, Physica B **329-333**, 313 (2003).

[54] M. Yamamoto, S. Higashitani, and K. Nagai, Physica B **329-333**, 301 (2003).

[55] J. V. Porto and J. M. Parpia, Phys. Rev. B **59**, 14583 (1999).

[56] D. T. Sprague, T. M. Haard, J. B. Kycia, M. R. Rand, Y. Lee, P. J. Hamot, and W. P. Halperin, Phys. Rev. Lett **75**, 661 (1995).

[57] H. Alles, J. J. Kaplinsky, P. S. Wootton, J. D. Reppy, and J. R. Hook, Physica B **255**, 1 (1998).

[58] D. T. Sprague, T. M. Haard, J. B. Kycia, M. R. Rand, Y. Lee, P. J. Hamot, and W. P. Halperin, Phys. Rev. Lett. **77**, 4568 (1996).

[59] K. Matsumoto, J. V. Porto, L. Pollack, E. N. Smith, T. L. Ho, and J. M. Parpia, Phys. Rev. Lett. **79**, 253 (1997).

[60] B. I. Barker, Y. Lee, L. Polukhina, D. D. Osheroff, L. W. Hrubesh, and J. F. Poco, Phys. Rev. Lett. **85**, 2148 (2000).

[61] N. W. Ashcroft and N. D. Mermin, *Solid state physics* (Saunders College Publishing, Orlando, 1976).

[62] W. Zhang, J. Kurkijärvi, and E. V. Thuneberg, Phys. Rev. B **36**, 1987 (1987).

[63] E. V. Thuneberg, Phys. Rev. B **36**, 3583 (1987).

Abstracts of publications

[P1] We study a two-phase sample of superfluid ^{3}He where vorticity exists in one phase (^{3}He-A) but cannot penetrate across the interfacial boundary to a second coherent phase (^{3}He-B). We calculate the bending of the vorticity into a surface vortex sheet on the interface and solve the internal structure of this new type of vortex sheet. The compression of the vorticity from three to two dimensions enforces a structure which is made up of $\frac{1}{2}$-quantum units, independently of the structure of the source vorticity in the bulk. These results are consistent with our NMR measurements.

[P2] We study theoretically the stability of flow in superfluid ^{3}He-A. The calculations are done using a one-dimensional model where the order parameter depends only on the coordinate in the direction of the superfluid velocity $\mathbf{v}_\mathrm{s}$. We concentrate on the case that the external magnetic field $\mathbf{H}$ is perpendicular to $\mathbf{v}_\mathrm{s}$, where only a few results are available analytically. We calculate the critical velocity v_c at which the superflow becomes unstable against the formation of continuous vortices. The detailed dependence of v_c on the temperature and on the form of the underlying orbital texture $\hat{\mathbf{l}}(\mathbf{r})$ is investigated. Both uniform and helical textures of $\hat{\mathbf{l}}(\mathbf{r})$ and two types of domain-wall structures are studied. The results are partially in agreement with experiments made in a rotating cylinder.

[P3] Superfluid ^{3}He-A has domain-wall-like structures, which are called solitons. We calculate numerically the structure of a splay soliton. We study the effect of solitons on the nuclear-magnetic-resonance spectrum by calculating the frequency shifts and the amplitudes of the soliton peaks for both longitudinal and transverse oscillations of magnetization. The effect of dissipation coming from normal-superfluid conversion and spin diffusion is calculated. The calculations are in good agreement with experiments, except a problem in the transverse resonance frequency of the splay soliton or in magnetic field dependence of reduced resonance frequencies.

[P4] This work is motivated by recent experiments studying superfluid ^{3}He inside porous aerogel. Using the homogeneous scattering model, we calculate the pairing amplitude and the superfluid density for the A and B phases at all temperatures. At high temperatures the results are in agreement with simpler calculations based on the Ginzburg-Landau theory. We also study the effect of large impurities in the B phase. We find that higher scattering channels give essentially the same results as obtained by limiting to s-wave scattering.

[P5] When aerogel is filled with ^{3}He the thin aerogel strands work as impurities and scatter the helium quasiparticles. These impurities cause a suppression in critical temperature, pair potential and superfluid density. The experimentally measured critical temperatures and superfluid densities for ^{3}He in aerogel can be fairly well explained by using an isotropic inhomogeneous scattering model where the impurity density is allowed to depend on location.

[P6] The standard treatment of impurities in metals assumes a homogeneous distribution of impurities. In this paper we study distributions that are inhomogeneous. We discuss in detail the "isotropic inhomogeneous scattering model" which takes into account the spatially varying scattering on the scale of the superfluid coherence length. On a large scale the model reduces to a homogeneous medium with renormalized parameter values. We apply the model to superfluid ^{3}He, where porous aerogel acts as the impurity. We calculate the transition temperature T_c, the order parameter, and the superfluid density. Both A- and B-like phases are considered. Two different types of behavior are identified for the temperature dependence of the order parameter. We compare the calculations with experiments on ^{3}He in aerogel. We find that most of the differences between experiments and the homogeneous theory can be explained by the inhomogeneous model. All our calculations are based on the quasiclassical theory of Fermi liquids. The parameters of this theory for superfluid ^{3}He in aerogel are discussed.